A Systematic Periodicity and Time-variable Modulation Search in RXTE ASM Data: Methods, Findings, and Implications for Astrophysical X-ray Sources

by

Robert J. Harris

Submitted to the Department of Physics
in partial fulfillment of the requirements for the degree of

Bachelor of Science in Physics

at the

MASSACHUSETTS INSTITUTE OF TECHNOLOGY

May 2007
[June 2007]

Author .....
Department of Physics
May 18, 2007

Certified by .....
Alan M. Levine
Principal Research Scientist
Thesis Supervisor

Accepted by .....
David Pritchard
Professor, Department of Physics

A Systematic Periodicity and Time-variable Modulation Search in RXTE ASM Data: Methods, Findings, and Implications for Astrophysical X-ray Sources

by

Robert J. Harris

Submitted to the Department of Physics
on May 18, 2007, in partial fulfillment of the
requirements for the degree of
Bachelor of Science in Physics

Abstract

In this work, we present the results of a general search for periodicities and for time-variable modulation strength in X-ray sources using data from the All-Sky Monitor onboard the Rossi X-ray Timing Explorer. New findings, including a sharp increase in the modulation of the X-ray flux from the Galactic bulge low-mass X-ray binary GX 9+9 and the recent spin-down event of the pulsar in the high-mass X-ray binary X0114+650, are reported. These searches employed new methods of periodicity detection that employed an algorithm to reduce the effects of low frequency noise from X-ray sources. We discuss these methods and show how they can be used to enhance the signal-to-noise ratio in the Fourier domain for many sources.

Thesis Supervisor: Alan M. Levine
Title: Principal Research Scientist

Acknowledgments

I would like to thank my research supervisor, Dr. Alan Levine, for his endless patience, helpful comments, and general good advice he has given me throughout my one and a half years of working with him. I also wish to thank Prof. Saul Rappaport for his support throughout my undergraduate career and especially his help with my graduate school applications. In addition, as I look back on my undergraduate years, I would like to thank my high-school mentors and friends who insisted that I attend, with special thanks to Mr. Tony Miller, Ms. Jan Young, Mr. John Woolley, and Mrs. Wanda Kuester. Without them, I surely would not be here now. Finally, I wish to thank my parents, Norris and Betty Harris. They have provided me endless support, encouragement, and love, and I owe them a debt I surely cannot repay.

THIS PAGE INTENTIONALLY LEFT BLANK

Contents

List of Figures

THIS PAGE INTENTIONALLY LEFT BLANK

Chapter 1

Introduction

X-ray astronomy began in 1949 when X-rays from the Sun were first detected by instruments onboard a V-2 rocket launched from the White Sands Missile Range in New Mexico (Tousey *et al.*, 1951). However, the study of extra-solar X-ray astronomy started in 1962 when a group at American Science & Engineering, led by Riccardo Giacconi, launched a rocket, during the flight of which X-rays from the brightest extra-solar X-ray source, Scorpius X-1, were observed (Giacconi *et al.*, 1962). Since that first discovery of extra-solar X-ray emission, X-ray astronomy has developed into a rich and vibrant field of astrophysics. What was once a region of the electromagnetic spectrum not available to astronomers has became a new tool to understand astrophyical objects: observations in the X-ray band yield important dynamical information about exotic systems ranging from binary systems with compact objects to clusters of galaxies.

In this chapter, I outline some of the objects thought to produce X-rays in significant quantities and review the mechanisms by which the X-ray production occurs. This discussion will lead to another on the ways that X-ray flux observed far away from these sources could vary with time. In the next two chapters, I give information on the X-ray instruments used to collect the data for this research (Chap. 2) and describe the methods I used to analyze the data for flux modulation and time-varying strength of such modulation (Chap. 3). I conclude with results, including those of a search for sources exhibiting periodicities detectable from an analysis of all data

available as of March, 2006, (Chap. 4), the peculiar case of a Galactic bulge X-ray source, GX 9+9, that instigated my search for time-varying modulation strength in other X-ray sources (Chap. 5), and the results of just such a search (Chap. 6).

1.1 Binary System Dynamics and Luminosity Generation in Binaries

Most of the X-ray sources that we will consider take the form of binary systems, and much of the X-ray emission from these sources derives from mass transfer from one star to another in these systems. Therefore, it is worthwhile to discuss the dynamics of binary orbits and how these dynamics combined with standard stellar evolution theory can lead to X-ray emission in these systems. In what follows, whenever I discuss a system including a compact object, I shall refer to the star that is not the compact star as the *companion star*. For some systems, I refer to the more massive star as the *primary star*, or just as the primary, and I refer to the less massive star as the *secondary* star, or just as the secondary.

We consider two idealized point masses, M_1 and M_2, that are separated by a distance r_{12} and are in a circular orbit around their common center of mass (CM) with distances from the CM of a_1 and a_2, respectively. Since they are in a circular orbit, the two masses orbit at some constant angular frequency ω. Because X-ray emission from these binaries depends crucially on mass falling onto the compact object from the companion, we consider the motion of a test mass. Since any mass transfer in the system is from the companion to the compact star, I focus on the case in which the test mass is at rest in the rotating frame in which the two stars are at rest. In the non-relativistic limit, the energy of such a test mass m at a distance r_1 from M_1, r_2 from M_2, and r from the CM, as observed in a non-rotating inertial frame at rest with respect to the CM is given by:

$$E_{CM} = -G\frac{M_1 m}{r_1} - G\frac{M_2 m}{r_2} + \frac{1}{2}m\omega^2 r^2. \tag{1.1}$$

where the first two terms are the gravitational potential energy terms due to the two stars and the third term is due to the circular motion of the test mass.

It is instructive to make a coordinate transformation into a frame in which all the bodies — the two stars and the test mass — are at rest. In transforming, we have to deal with two new forces: the "centrifugal force" and the Coriolis force. The first is described by a potential-like term. The second, however, is not. The Coriolis force is given by $\vec{F_C} = -2m\vec{\omega} \times \vec{v}_{\rm rot}$. where $\vec{v}_{\rm rot}$ is the velocity of the test mass in the rotating frame and $\vec{\omega}$ is the angular velocity vector of the system. This force ensures that the total angular momentum of the system is conserved, and it turns out that this term is responsible for the creation of "accretion disks" made of the infalling material of the companion which orbits around the compact object for a time. These disks are described in more detail below. Because this force's primary role is in creating accretion disks and not in the first stages of mass transfer, we ignore it for now.

Transforming the energy equation into the rotating frame and dividing by the test mass, one obtains an effective gravitational potential for points in the vicinity of the binary system. This is given by:

$$\Phi_{\rm eff} = -G\frac{M_1}{r_1} - G\frac{M_2}{r_2} + \frac{1}{2}\omega^2 r^2, \tag{1.2}$$

Because of this additional harmonic oscillator term, the equipotentials are not those of two gravitating objects at rest. As an example, the equipotentials for the effective gravitational potential of a system in which the mass ratio of secondary to primary is $q = 0.4$ are shown in Fig. 1.1 in which the primary is at the origin and the secondary at $x = 0$, $y = 1$.

In Fig. 1.1, one notices the "figure 8" that surrounds both the stars. The point at the intersection of the curve is point of unstable equilibrium of a test mass at rest with respect to the stars in the rotating frame. It is called L_1, or the first Lagrange point. There are four other unstable equilibria, labeled L_2 through L_5 (Carroll and Ostlie, 1996). This is a general result for all binaries. The lobes formed by the figure 8 are called the *Roche lobes*, and they form a sort of critical boundary for test particles

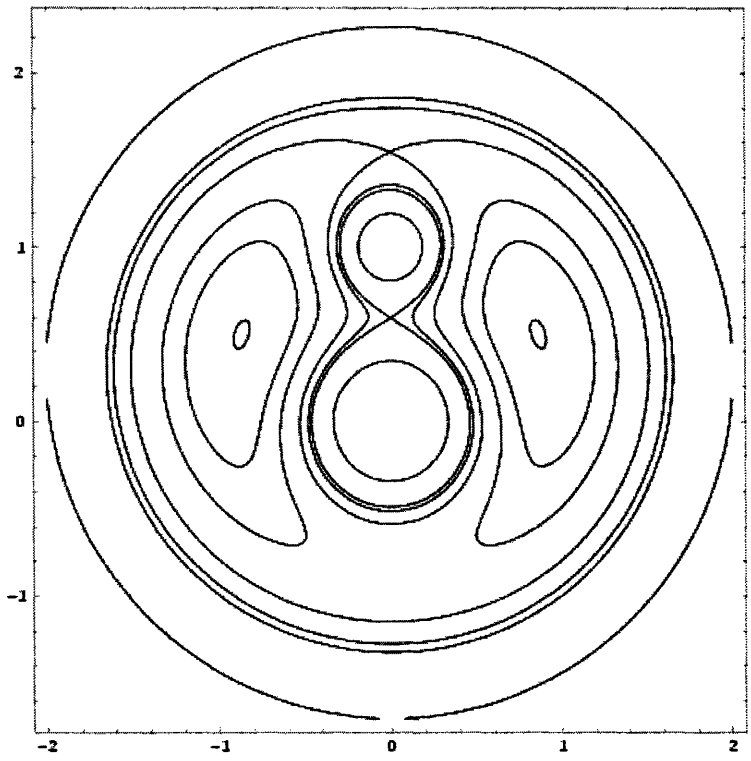

Figure 1-1: Cross section of equipotential surfaces in the orbital plane of a binary with circular orbit and $q = 0.4$. Tickmarks along the axis have been normalized to the orbital separation, so a = 1. (Benacquista, 2002)

in the vicinity of the system. If a test particle is placed at rest in the rotating frame of the binary and within the Roche lobe of one object, say M_1, it will be attracted towards M_1. Similarly, if the particle is placed outside the Roche lobe of M_1, it will be repelled from M_1 and, depending on where the particle is initally placed, may end up being attracted towards M_2.

In X-ray producing binary systems, the X-ray luminosity is thought to be generated by matter from the companion star. One possible mechanism for this luminosity is called *Roche lobe overflow.* To demonstrate this mechanism, consider a normal-type star in orbit around a compact object. As the companion evolves, stellar evolution theory informs us that its radius increases. Since the mass of the star remains roughly constant during the star's radial expansion, the average distance of the companion star's Roche lobe from the center of the companion, referred to as the star's Roche lobe radius, remains constant, as the Roche lobe radius is fixed by the mass ratio of the system. Specifically, for systems in which the ratio of companion mass to compact object mass is q, Paczyński (1971) fit the following formula to numerical simulations, where the Roche lobe radius, R_L, is expressed in terms of the orbital separation a:

$$R_L/a = \begin{cases} 0.462\left(\frac{q}{1+q}\right)^{1/3} & 0 < q < 0.8 \\ 0.38 + 0.2\log q & 0.3 < q < 20. \end{cases} \quad (1.3)$$

Therefore, as the star expands, its radius may exceed that of the Roche lobe.

If overflow happens, some of the gas from the companion's envelope that is outside of the lobe tends to be attracted towards the compact object. The gas passes through the inner Lagrange point L_1. Viscous forces within the hot plasma cause loss of both energy and angular momentum in the material so the material starts to insprial towards the compact object. If the magnetic field of the compact object is weak, as in the case of non-pulsating neutron stars and black holes (which posess no magnetic fields), the material tends to form an *accretion disk* around the compact object. Viscous forces in the disk cause heating and loss of angular momentum, and, as angular momentum is lost, the accreting material falls deeper into the potential well

of the compact object. This gas heats as it falls into the well, and this heating is thought to cause a significant portion of the X-ray flux from an X-ray producing binary. As the orbit decays, the end-point of the accreting material's journey depends on the type of compact object. If the object is a black hole, then the accretion disk will orbit around the black hole until it reaches the innermost stable circular orbit, located at three Schwarzchild radii away from the black hole, at $r = 6GM_{\rm BH}/c^2$. Any material making its way through the disk to past this radius will fall into the event horizon, yielding no more luminosity. Therefore, in black-hole systems, the X-ray luminosity mechanism is through cooling of the accretion disk by emission of radiation. For a rest mass accretion rate $\dot{M}$, this results in a luminosity $L_{\rm X} \approx 0.1\dot{M}c^2$. If the compact object is a weakly magnetized neutron star, the orbit of the material in the accretion disk decays until it collides with the compact object. In this collision, the kinetic energy of the material, deriving from the material's gravitational potential energy, is liberated as heat and electromagnetic radiation. A rough estimate of the luminosity generated in the collision is given by equating the Newtonian gravitational potential energy of a test mass m infinitely far away from the source, representing the material falling onto the neutron star from the companion, to the kinetic energy obtained by the source when it free falls to the surface of the neutron star. This is given by

$$\frac{GM_{\rm NS}m}{R} = \frac{1}{2}mv^2. \tag{1.4}$$

For a canonical neutron star mass of $1.44M_\odot$ and radius 10 km, the Newtonian calculation results in a velocity $0.54c$, and that velocity implies a Lorentz factor $\gamma = 1.19$. Thus, if all the kinetic energy of the object was transformed to heat and light upon impact, this rough calculation implies a yield of energy of $\sim 0.2mc^2$. In reality, the luminosity accompanying accretion is given by $L = (0.2 - 0.3)\dot{M}c^2$. For a black hole, the luminosity tends to be $L \approx 0.1M_\odot c^2$.

Other than by accretion via Roche lobe overflow, X-ray luminosity may also be generated by accretion of a companion star's strong stellar wind without the need for an accretion disk. However, the efficiency of this process tends to be much lower. The

physical reasoning for this comes from the fact that, in the rotating frame in which the binary system is at rest, a stellar wind tends to be driven away from the companion in an approximately spherically symmetric manner, so the compact object, which due to its size subtends a small solid angle on the sky when it is viewed from the companion star, only captures a small fraction of the wind. Roche lobe overflow, on the other hand, tends to direct the mass flow through L_1 and into the region dominated by the compact object's gravity.

Having described in some detail the orbital dynamics of binary systems and how the dynamics lead to X-ray production, we are now in a position to discuss how this X-ray flux is modulated in the systems we observe. Studying flux modulation in X-ray sources can provide important details about the systems from which the flux originates, such as the orbital period of a binary, an accretion disk precession period, or a neutron star spin period, and these are the interesting phenomena that one might wish to learn more about through studying the lightcurves of X-ray sources.

1.2 Types of Modulation of X-ray Flux

The lightcurves of X-ray sources exhibit a wide variety of behaviors that range from that of some transients whose X-ray luminosity is "on" for a while and then "off" for a time to those of eclipsing sources in which, once every orbital cycle, the companion star blocks the line of sight to the compact object which is emitting X-rays. We review below the different classes of X-ray modulation and their underlying physical mechanisms.

1.2.1 Eclipses and Dips

Eclipses and dips both derive from periodic obscuration of all or part of an X-ray emitting region. Eclipses of a central X-ray source by the companion star or by the accretion disk result from total blocking of the source along the line of sight and tend to yield almost totally complete obscuration. However, the explanations for dipping

are more varied. Dipping can arise from an increase in the column density along the line of sight resulting either from accretion disk instabilities or from a "splashing up" of material from the contact point of the accretion stream and disk. This reasoning seems to indicate that, perturbations to the entire structure of the system aside, dipping events should be more irregular than eclipse events, as irregular eclipsing events would imply some sort of disruption to the overall structure of the source. Indeed, this prediction coincides with what we observe. In dipping sources such as X1254-690, pointed observations using the PCA have shown that sometimes dips do not materialize when they are expected (or at all) during an observation of length on the order of a day (Smale and Wachter, 1999). However, the author is unaware of sources for which changes in flux modulation strength are attributable to varying eclipses of the central source.

1.2.2 X-ray Pulsations

X-ray pulsars are those accreting neutron stars in X-ray binaries that rotate with periods on the order of hundreds or thousands of seconds down to milliseconds. Strong magnetic fields cause accreting material to be channelled along the flux lines onto "hot spots" that coincide with a magnetic pole of the neutron star. The neutron star's rotation causes the hot spot(s) on the neutron star to point along the line of sight once or twice — depending on whether the accretion flows onto one or both magnetic poles — per rotation of the neutron star. The magnetic field also causes the opacity profile near the hot spot to be anisotropic, so that the opacity along a line extending radially from the hot spot on the star is less than along other lines extending from the hot spot. The two effects — the hot spot and the anisotropic opacity profile — cause a beaming of radation, called the pulsar's pulsation. We call that period the pulse period. Long term monitoring can observe changes in the pulse period. Both changes resulting in period increases and those resulting in period decreases are thought to derive from torques in the accretion flow that are only partly understood. Aside from the relatively slow spin-up and spin-down mechanisms due to accretion flows, there are apparently mechanisms whereby pulsars may suddenly spin-up or spin-down.

These events, called "glitches," have been observed in a wide variety of radio pulsars and in so-called anomalous X-ray pulsars (AXPs). The currently favored mechanism by which these glitches occur is through sudden angular momentum transport from superfluid vortices in the neutron star's core to the star's surface, as expounded on in, e.g., Ruderman (1976).

1.2.3 X-ray Bursts

Sharp increases in the intensity of the X-ray flux from various sources can be seen in bursting sources. The existence of such bursting sources is of interest for two reasons. First, regular bursting can yield a period characteristic of a system, such as a timescale for accretion events. Second, irregular bursting can cause noise in the Fourier spectrum of a source, and this noise can obscure the signal of, e.g., a shallow periodic dip that might be present in the data.

X-ray bursting sources are divided into two groups, type-1 X-ray burst sources and type-2 X-ray burst sources. Type-1 X-ray bursts originate from uncontrolled nuclear burning on neutron stars. For neutron stars with weak magnetic fields, the accreting material does not concentrate in one hot spot on the surface of the star. Instead, after the impact of the material onto the surface, the accreted hydrogen tends to spread out over the surface. In the lower layers of the accreted material, nuclear fusion caused by the pressure of the upper layers turns hydrogen into helium. As more H accumulates, upper layers of H can cause enough pressure on the lower layers, where H has already been fused into He, to start uncontrolled nuclear burning of the He layers. The resultant burning causes a flash of X-rays which is the type-1 X-ray burst. Since black holes have no such surface as a neutron star has, no type-1 bursts are expected from black hole candidates (BHCs). In white dwarfs, a similar process can also occur, although it happens much less frequently than it occurs with neutron stars. In the case of the white dwarf, the flash of X-rays (and accompanying optical burst) is called a nova.

Type-2 X-ray bursts are thought to result from fast accretion events of short duration. In other words, in some short time interval (on the order of one to tens

of seconds), some amount of material is accreted from the companion, and then accretion stops. In sources with periodic type-2 bursts, the bursts occur at intervals of anywhere from 7 sec to 1 hour. Both types of X-ray burst tend to originate from either thermonuclear flashes or spasmodic accretion, and the spectra of the bursters tend to be dominated by a thermal blackbody component.

Finally, having completed a discussion of the ways that mass transfer, and by extension X-ray generation, occurs in binary systems, as well as how the X-ray flux from such systems may be modulated, we are finally ready to introduce the types of astrophysical X-ray sources we will see during this research.

1.3 Astrophysical X-ray Sources

1.3.1 X-ray Binaries

One of the principal astrophysical systems that can produce X-rays is the *binary* system. Note that not all binaries produce X-rays in copious amounts. Rather, X-ray producing binary systems typically comprise a normal-type star and a compact object. For binary systems to produce X-rays, they must typically have very close orbits, as is implied by the requirements of large-scale mass transfer as previously explained. Those X-ray producing binary systems in which the compact object is a black hole or neutron star are called *X-ray binaries*, and they are divided into two categories based on the mass of the normal-type star. The two categories are the *high-mass X-ray binaries* and the *low-mass X-ray binaries.* The characteristics of each class are discussed below.

High-mass X-ray Binaries

HMXBs are comprised of a normal-type O or B star with a mass on the order of $M \gtrsim 5M_{\odot}$ in a binary system with either a neutron star or a black hole. There are two subclassifications of HMXBs. The first grouping is composed of those HMXBs

with a Be star secondary. Be stars are B class stars whose spectra are dominated by strong HI emission and that tend to rotate rapidly enough to form a flattened bulge around their equator. The second subclassification of HMXBs is composed of those with a supergiant (SG) secondary. (Lewin *et al.*, 1997)

Be/X-ray binaries comprise the majority of HMXBs, and a majority of these systems house pulsars (Ziolkowski, 2002). They are also called *hard X-ray transients* because their spectrum is hard ($k_BT \gtrsim 15$ keV) and because their X-ray emission tends to be transient. This transience comes in two forms. First, the flattened bulge, a disk of stellar wind around the Be star, is unstable and disperses on a timescale of years while the accretion disk around the neutron star is found to do so on a timescale of weeks. The evolution of the disks leads to both type-1 and type-2 X-ray outbursts. These outbursts dominate the X-ray luminosity of a Be/X-ray binary system. Periodic type-1 outbursts owe their existence to the fact that the orbital plane of the neutron star does not coincide with the equatorial plane of the Be star. This fact combined with their fairly eccentric orbits ($0.1 < e < 0.9$) cause the neutron star to "flick" the Be star bulge, causing fast accretion events to occur at every passage through periastron, though in some cases these outbursts are missing from some periastra in a source's lightcurve (Ziolkowski, 2002). type-2 outbursts are more irregular than the periodic type-1 outbursts, and they also cause higher X-ray luminosity than their type-1 cousins. The cause of the type-2 outbursts is not well understood, though they are thought to be caused by an cyclical emptying and refilling of the decretion disk around the Be star. These cyclical events are thought to cause irregular events wherein large amounts of material from the Be star flows onto the neutron star, causing large increases in X-ray luminosity.

SG/X-ray binaries comprise a supergiant and a compact object. Their X-ray luminosity is thought to derive from one of two sources. The first is Roche lobe overflow. The second source thought to be responsible is a strong stellar wind driven away from the surface of the supergiant. As mentioned above, Roche lobe overflow tends to direct more of the mass flow towards the primary. Therefore, the wind-driven mechanism results in a much lower luminosity ($L_x^{\rm wind} \sim 10^{36}$ ergs sec^{-1}) than

the overflow mechanism ($L_x^{\text{Roche}} \sim 10^{38}$ ergs sec^{-1}). The SG/HMXBs tend to be persistent sources, as contrasted to the Be/HMXBs. (Ziolkowski, 2002)

Periodicities in the X-ray flux from HMXBs are relatively easy to detect, especially compared to those in the flux of their low-mass cousins. This is in part due to the fact that the companions of HMXBs are typically much larger than than those in LMXBs, so, for a compact object of a given radius, a wider range of orbital inclination angles lead to observable eclipses and/or dips in HMXBs than in LMXBs. Since the primaries tend to be large, the periods of HMXB orbits tend to be longish (tens to hundreds of hours) as compared to those of their LMXB cousins (one to ten hours).

Low-mass X-ray Binaries

LMXBs are comprised of a later-type star (typically later than A) of mass $M \lesssim 2$ $M_\odot$ and a neutron star or black hole. These systems' X-ray luminosities are not powered by stellar winds, but rather by Roche lobe overflow of the companion onto the compact object. (Lewin *et al.*, 1997)

The primary classification scheme for LMXBs is not based on the type of star the companion is, as in HMXBs, but it is instead based on the phenomenology of the X-ray spectrum that the source emits. To describe the two different classifications, we must make a digression to describe a type of astronomical diagram.

Color-Color Diagrams

One coarse representation of the X-ray spectrum of a source is given by what are called *colors*. A color is defined to be a ratio of X-ray counts detected in one energy band, B, to those in another, A, where the energies of the X-rays in band B are higher than those in band A. One can derive what is called a *hard color* which is a ratio of, e.g., the number of photons received at a detector with photon energy E_γ between 15 and 20 keV to the number of photons with E_γ between 10 and 15 keV. We can also define a *soft color* similarly, but with lower energies used for the bands, e.g. 5-10 keV and 1-5 keV. For each time-bin of the observation, we may then plot the hard color versus the soft color. The plot is called a *color-color* diagram.

Note that we may also plot many different combinations of variables of interest.

Other than color-color diagrams, those used most often are color-intensity diagrams where either the hard or the soft color is plotted against the intensity of the source. These diagrams can provide valuable diagnostics on the nature of the source.

Two types of LMXBs containing neutron stars are currently known: the *Z sources* and the *atoll sources.* The difference between the two lies both in the shape that they trace in the color-color diagram over time and the timing properties of the two types of sources.

The Z sources are those neutron star containing LMXBs that trace out a **Z**-shaped pattern in the color-color diagram. Typically, the Z sources trace out a Z smoothly in a matter of either hours or days, and the time of tracing does not usually seem to be correlated with an orbital or spin period in the system (Muno *et al.*, 2002). These sources typically exhibit quasi-periodic oscillations (QPOs) with frequencies on the order of 1-60 Hz, and they typically have broadband noise at low frequencies in the Fourier domain (Muno *et al.*, 2002). Their fast time variability is strongly correlated with the location of the source in the "Z." Kilohertz QPOs are also detected in the Z sources, and their frequencies increase with increasing luminosity and, hence, increasing $\dot{M}$. They are typically much more luminous in the X-ray band than the atoll sources and are thought to be Eddington-limited.

One should contrast the behavior of the Z sources with those of the atoll sources. Rather than tracing out a continuous shape, the atoll sources typically show many "islands" of points. Their power spectral properties at a given time are correlated with which island they reside in at the time, with strong band-limited noise detected in some locations in the color-color diagram and not in others. Kilohertz QPOs are also detected in these sources, usually in pairs where the frequencies increase with increasing $\dot{M}$. The differences in both timing and spectral behavior are believed to be due to large differences in $\dot{M}$ among the atoll sources.

Cataclysmic Variables

Cataclysmic variables, or CVs, are close orbit binary systems ($P \lesssim 0.1$ days typically) in which the secondary is a late-type M or K dwarf star and the secondary is an accreting white dwarf. Roughly, one classification scheme is organized by the strength of the magnetic field that the compact object possesses. First, we consider the AM Herculis type CVs, also called polars. In these systems, the magnetic field at the surface of the accretor approaches a few megagauss. The secondary overfills its Roche lobe, but once material starts infalling onto the white dwarf, the strong magnetic field of the polar disrupts any accretion disk even out to the first Lagrange point and prevents the disk from forming. Instead of mass transfer via accretion disks, mass from the secondary moves along the flux lines of the white dwarf and is guided into a tiny area that coincides with one of the magnetic poles of the dwarf. The X-ray luminosity derives from the kinetic energy of the accretion flow, which is converted to electromagnetic radiation via bremsstrahlung radiation upon impact, and from viscous forces in the accretion stream itself. Also in AM Her type CVs, there is a phase-locking between the white dwarf's spin and the orbit because of the strong magnetic field. (Lewin *et al.*, 1997)

CVs that include slightly less magnetic white dwarfs ($B \sim 1$ megagauss) are referred to as either DQ Herculis stars after the archetypal example for this subclass or as intermediate polars. In these systems, Roche lobe overflow of the secondary causes an accretion disk to form around the accretor, but the strong magnetic field of the white dwarf disrupts the accretion disk interior to some radius from the dwarf and causes matter to follow the magnetic field lines towards the poles of the accretor. The resultant X-ray luminosity is due to the same sources as in the case of AM Her type CVs. QPOs are occasionally observed in these sources. Lewin *et al.* (1997)

The other large classification of CVs includes the dwarf novae. In these systems, the magnetic field of the white dwarf is small compared to those of the other two types of CVs, lending these to the formation of accretion disks as in LMXBs and some HMXBs. In these cases, the basic physics of the accretion process is similar

enough to that in the X-ray binaries not to merit further attention.

Having reviewed the physical processes at work most often in high energy astrophysics, and the astronomical objects we wish to study, we shall next overview the relevant facts about the instrumentation onboard the Rossi X-ray Timing Explorer that was used in observing sources in which we are interested. These are the All-Sky Monitor (ASM) and the Proportional Counter Array (PCA).

THIS PAGE INTENTIONALLY LEFT BLANK

Chapter 2

Instrumentation

The Rossi X-ray Timing Explorer (hereafter, RXTE) has collected data on the X-ray sky continuously since early 1996 (Levine *et al.*, 1996). Onboard are three observing instruments: the All-Sky Monitor (ASM), the Proportional Counter Array (PCA), and the High Energy X-ray Timing Experiment (HEXTE). During the research described in this work, we have used data from the first two instruments. Their specifications and workings are outlined below.

2.1 All-Sky Monitor

The ASM's main mission is to observe X-ray sources to monitor for large changes in either their intensity or their spectrum so as to provide an early-warning system so that scientists might use other instruments, based either on the ground or in space, for pointed observations of such sources in the immediate aftermath of such changes. Because of the long-term monitoring required for this mission, ASM data are ideally suited for searches for periodicities with frequencies ranging from several minutes to days or even years.

The ASM consists of three scanning shadow cameras (SSCs) mounted on a frame that can rotate fully 360° around its drive axis. Each SSC houses a position sensitive proportional counter filled with xenon and carbon dioxide gasses. To reach the proportional counter, X-rays must travel through slits on a mask that covers the cam-

era. The photons enter the gas chamber inside the proportional counter and ionize the gas inside, where the strength of ionization is directly correlated with the energy of the photon. Voltages applied to eight carbon-coated quartz-fiber anodes in the proportional counter cause an electric field to be created that is radial to the anode. The free electrons that are liberated by the absorption of the X-ray photons are attracted by this electric field and strike the anode. This interaction of the electrons with the anode causes a pair of voltage pulses which travel to opposite ends of the anode. Their sizes are then used to determine the energies of the electrons as well the locations along the anode where the incident electrons struck. Note that the propogation of these pulses depends crucially on the characteristics of the anode, most importantly the profile of resistivity along the length of the anode. Much work has gone into modelling the changes in resistivity in time since the launch of the mission. This work has benefitted greatly from a major calibration effort undertaken within the past year by Dr. Alan Levine to correct data for degradation of the anodes. A schematic of the ASM is shown in Figure 2-1.

The X-ray events – their locations along the anode and their energies – are analyzed by the event analyzers (EAs) assigned to the ASM. During each 90 second dwell, the EAs record the count rate as measured in the above fashion. Before 2000, the EAs had accumulated histograms of counts versus position along the anode and then sent these histograms back to the ground. Since 2000, the EAs have sent the data on each individual event down to the ground, and the histogram has been accumulated on the ground using these data. During each dwell, the number of counts in each of three energy bands, the A band ($1-3$ keV), the B band ($3-5$ keV), and the C band ($5-12$ keV), are accumulated separately. The histogram that results from each dwell's data is fitted against a model histogram that uses as parameters the intensity of each source known to be in the field of view of the cameras during the dwell. If it is suspected that a source previously undetected by the ASM exhibits a signature in the histogram, methods can be applied to test this. Typically, shadow patterns caused by sources at different locations in the field of view of the cameras are generated, and they are each fit against the residuals of the histogram — the residuals being

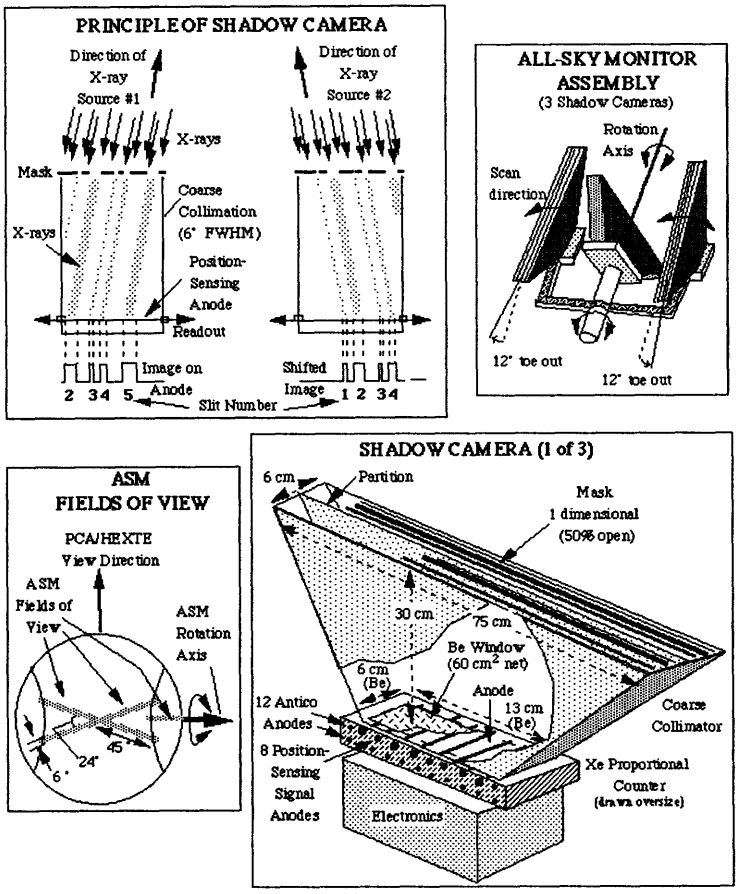

Fig. M: ASM

Figure 2-1: SSC and ASM schematic.

calculated by taking the original histogram and subtracting the best-fit histogram that is fit for all sources previously detected by the ASM that are in the field of view. Typically, the sensitivity limit for such detections is $\sim$ 50 mCrab. The precision of the ASM for previously undiscovered sources yields an error box of approximately $0.2° \times 1°$ for sources at about the 50 mCrab level, but the ASM can, for sufficiently bright sources, reach a precision of 1 arcminute.

The cameras have a field of view of $6° \times 90°$ at FWHM. After each dwell, the drive assembly rotates the three SSCs by approximately 6°. During one rotation of the ASM – taking approximately 100 minutes – it is able to observe approximately 80 percent of the sky. This makes it likely that most of the X-ray sky — with the exception of that near the Sun — is observed during the day. The limiting sensitivity of the ASM is approximately 10 mCrab for 1 day of observation. The collecting area of the ASM is approximately 30 cm^2 per SSC with the mask on.

2.2 Proportional Counter Array

The PCA is the primary instrument on the RXTE that provides pointed observations of X-ray sources. It has capabilities of both fast-timing and spectral analyses, providing sensitivity to X-rays with energies of up to 60 keV. It was instrumental in the discovery of both kilohertz quasiperiodic oscillations from X-ray binaries as well as in the discovery of millisecond X-ray pulsars.

The PCA consists of 5 proportional counters with a combined effective collecting area of $\sim$ 6500 cm^2. The 5 proportional counter units (PCUs) view the sky through hexagonal collimators that provide collimation of 1° (FWHM). Each PCU contains five layers: one propane veto layer, three xenon/methane layers, and one xenon veto layer. This results in nine signal chains, two from each of the Xe/methane layers, two anticoincidence channels that prevent X-rays from being double-counted in the detector (one in the initial propane layer and the other in the Xe layer), and one calibration channel used for calibration of the instrument with X-rays emitted by an on-board Am-241 source. The end of the PCA signal chain lies in the Experiment

Data System (EDS). The EDS tags each X-ray photon to 1 μsec precision and processes it with six event analyzers. Two EA modes are employed for most purposes. These are the timing mode (also called the Standard 1 mode) which provides time-resolution of $\Delta t = 1/8$ sec and the spectral mode (also called the Standard 2 mode) for which $\Delta t = 16$ sec. For all PCA observations mentioned in this work, the spectral mode has been selected.

Over the course of the mission, the PCA has undergone 5 "gain epochs." During a single gain epoch, the calibration of the Standard 2 channels is roughly constant. However, the gain on each PCU has been changed four times because of instrumental problems. Also, additional gain calibrations are done by studying the Crab Nebula and asserting that its colors must be constant.

Now that we have described the instruments we have used to obtain data on different astronomical X-ray sources, we turn to the methods we have used to analyze this data and determine whether periodic modulation exists in the X-ray flux. In employing new methods of periodicity detection, we hope to improve the S/N-ratio in the Fourier domain of the ASM.

THIS PAGE INTENTIONALLY LEFT BLANK

Chapter 3

Data Products and Analysis

In this chapter, we discuss the methods we used to analyze ASM data for periodicities and time-variable modulation strength. We also comment on previous work that used ASM data to search for X-ray periodicities.

3.1 Periodicity Detection

Given an astronomical time series, there are multiple ways to determine whether it contains a periodic modulation. Among the most useful is the Fourier transform. The Fourier transform and the problems in applying Fourier techniques to ASM data are discussed below.

3.1.1 Fourier Methods

Suppose we are given a time series $x[t_i]$ where $t_{i+1} - t_i = \Delta t$, with Δt constant and i ranging from 0 to $N-1$. Then the *discrete Fourier transform*, or DFT, of $x[t_i]$, referred to by $\bar{x}[\nu_k]$, is given by

$$\bar{x}[\nu_k] = \sum_{i=0}^{N-1} x[t_i] e^{-2\pi j \nu_k t_i / N}, \tag{3.1}$$

where $j = \sqrt{-1}$.

It can be shown that any time series $x[t_i]$ can be uniquely decomposed into components of the form $\exp(2\pi j\nu_k t_i/N)$, where $\nu_k = k/(N\Delta t)$ and k runs from 0 to $N-1$, i.e., that every time-series has a unique frequency decomposition. This fact depends on the existence of an inverse DFT.

That each time-series has a unique DFT that represents its frequency decomposition is obviously of importance in what we are seeking to accomplish – to detect and characterize periodicities in X-ray sources. Most often, we will characterize the time-series not by its Fourier transform, but by its power density spectrum, $P[\nu_k]$, where $P[\nu_k] = |\bar{x}[\nu_k]|^2$

It is of note that, since all of our time-series will be real-valued, $\bar{x}[\nu_k] = \bar{x}^*[\nu_{N-1-k}]$ where * denotes complex conjugation. Since this is true, ν_{N-1-k} is interpreted as the additive inverse of νk, and we will refer to ν_{N-1-k} as $-\nu_k$ Therefore, $P[\nu_k] = P[-\nu_k]$ for our purposes, and we will always, when presenting power spectra, redefine the power at frequency ν_k as the sum of that at ν_k and that at $-\nu_k$.

When a time-series is obtained from any astronomical detector, what is recorded is not the source's true signal; the true signal would be a continuous data set. Because of sampling, what we observe is the time-series $x[t_i] = w[t_i]s[t_i]$, where $w[t_i]$ is the so-called "window function," defined to be 1 when the source is being observed and 0 when it is not, and where $s[t_i]$ is the true time-averaged source strength in time-bin t_i. When one computes a Fourier transform of $x[t_i]$, the result is the convolution of the Fourier transforms of $s[t_i]$ and $w[t_i]$. We see this by considering the convolution of the two Fourier transforms. For clarity, since the indices on all the summations below run from 0 to $N-1$, I have removed the bounds on the dummy indices from

the summations.

$$
\begin{aligned}
(\bar{w} \otimes \bar{s})[\nu_k] &= \sum_l \bar{w}[\nu_l]\bar{s}[\nu_k - \nu_l] \\
&= \sum_l \sum_m \sum_i w[t_i]s[t_m] \exp\left(-2\pi j(\nu_k - \nu_l)t_i/N\right) \exp\left(-2\pi j\nu_l t_m/N\right) \\
&= \sum_m \sum_i w[t_i]s[t_m] \sum_l \exp\left(-2\pi j\nu_k t_i/N\right) \exp\left(-2\pi j\nu_l(t_m - t_i)\right) \\
&= \sum_m \sum_i w[t_i]s[t_m] \exp\left(-2\pi j\nu_k t_i/N\right) \delta_{im} \\
&= \sum_i w[t_i]s[t_i] \exp\left(-2\pi j\nu_k t_i/N\right) \\
&= (\bar{sw})[\nu_k] \\
&= \bar{x}[\nu_k]
\end{aligned}
$$

The operator $\otimes$ denotes the discrete convolution. Note that what we really would like is $\bar{s}[\nu_k]$ since it alone and not $\bar{w}[\nu_k]$ contains information on the source. Unfortunately, it is not, in general, possible to define uniquely a de-convolution. In other words, there no well-defined operation $\otimes^{-1}$ such that $(\bar{w} \otimes^{-1} \bar{x})[\nu_k] = \bar{s}[\nu_k]$. This means that we are somehow going to have to deal with the effects of convolution.

This, however, sounds easier than it is. In Fig. 3-1, we present power density spectra of both the window function of a source and the source's intensity detected by the ASM. One should note the striking similarities between the two as exemplified by both specta's large DC levels, their spikes at 1 cycle day^{-1}, those at 15 cycles day^{-1}, and those at their harmonics and beats. These artifacts in the PDS derive from the effects of the rotation of the Earth (for 1 cycle day^{-1}) and the orbit of the satellite (15 cycles day^{-1}). These, notably, are the frequencies that dominate the window function, since the instruments onboard the RXTE are turned off roughly once per orbit due to radiation from the van Allen belts, particularly in the South Atlantic Anomaly, and since a source would be expected to be blocked by the Earth once per orbit. Note that the small signal present at $\sim$ 5 cycles per day in the source's spectrum is dominated by the large spikes. In fact, these spikes introduce

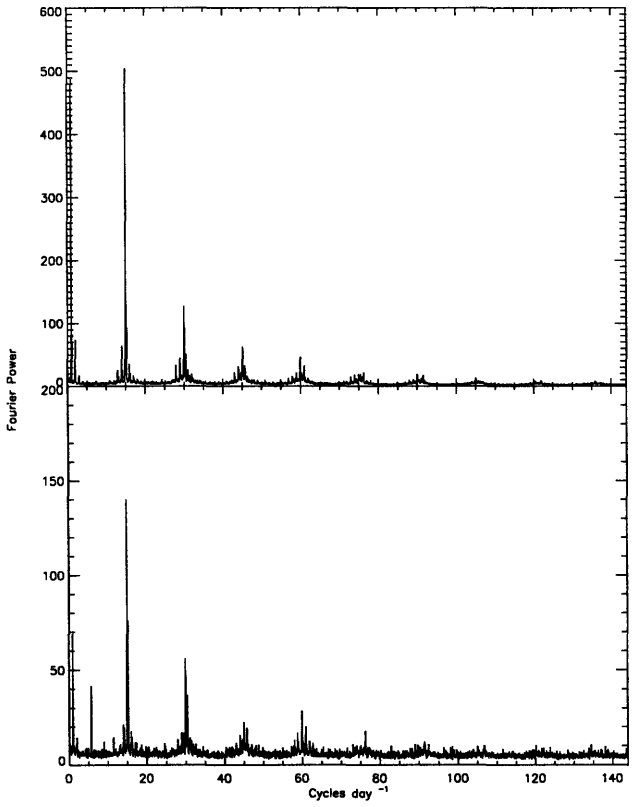

Figure 3-1: Power Density Spectra of window function and sum band X-ray flux of GX 9+9. The upper plot is that of the window function, while the lower one is that of the source intensity.

noise throughout the PDS through the effects of convolution; I will describe these effects below, but first it makes sense to illustrate the effect of the window function on the PDS we observe. To do this, we plot both the window function ($w[t_i]$ in the discussion above) PDS and the PDS of the source intensity modulated by the window function ($x[t_i]$ in the discussion above) in Fig. 3-1 for the X-ray source GX 9+9. One should note that in both plots, the DC power level goes well above the top of the plots. For instance, the window function DC power is on the order of 2×10^5.

Why are the features of the window function so evident in the source PDS? X-ray sources typically have a large amount of spectral power in lower frequencies, i.e., they

exhibit noise with shades of pink and red. The presense of such noise dominated by low frequencies leads to contamination of the PDS we calculate. This contamination derives from the window function.

To explain how this works, we have to consider the effect of convolution. For the sake of clarity, we focus on the case of continuous convolution of two functions, as discrete convolution can be obtained just by substituting δ-functions of appropriate equivalent area for the functions being convolved. For two functions of frequency, $f(\nu)$ and $g(\nu)$, the convolution $f \otimes g$ is another function of frequency, and it is defined by the equation

$$(f \otimes g)(\nu) = \int_{-\infty}^{\infty} f(\nu' - \nu) g(\nu') d\nu'. \tag{3.2}$$

This function measures the "overlap" between the functions f and g as a function of ν, where f has been reversed in frequency and shifted along the frequency-axis by the argument, ν. It is of note that the integral is symmetric in f and g, as is hinted at by the explanation of convolution in terms of an overlap.

To illustrate the effects of convolution, we work out an example. Suppose that we have a signal $s(t)$, the Fourier transform of which is given by the function

$$\bar{s}(\nu) = \begin{cases} 10 & |\nu| < \nu_{\text{char}} \\ \epsilon & |\nu| < 3 \pm \gamma \\ 0 & \text{otherwise,} \end{cases} \tag{3.3}$$

and a window function $w(t)$ whose Fourier transform is a δ-function train:

$$\bar{w}[\nu] = \delta(\nu) + \frac{1}{2}\delta(\nu \pm 1) + \frac{1}{4}\delta(\nu \pm 15). \tag{3.4}$$

The frequency-domain function $\bar{s}(\nu)$ represents a function in the time-domain that has signifcant low frequency noise of width ν_{char} and a signal at a (dimensionless) frequency $\nu = 3$ with width γ. The function $\bar{w}(\nu)$ represents a window function with strong frequency components at $\nu = 1$ and 15 and strong DC component. The convolution integral picks out the δ-functions, and the expression for the convolution

reads

$$\bar{s} \otimes \bar{w}(\nu) = \bar{s}(\nu) + \frac{1}{2}\bar{s}(\nu \pm 1) + \frac{1}{4}\bar{s}(\nu \pm 15). \tag{3.5}$$

The functions $\bar{w}(\nu)$ and $\bar{s}(\nu)$ are shown in Fig.3-2 and Fig. 3-3 for $\nu_{\rm char} = 0.05$, $\epsilon = 0.1$, and $\gamma = 0.001$. The convolution of the two functions is shown in Fig. 3-4.

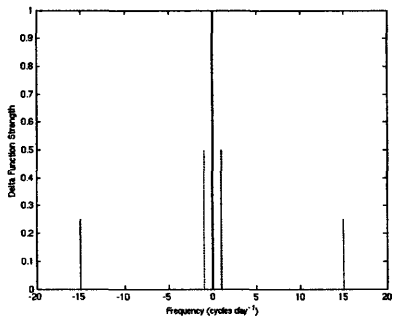

Figure 3-2: Example of Fourier transform of a window function.

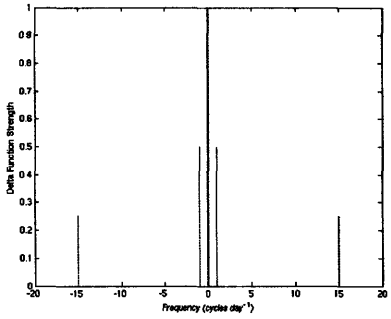

Figure 3-3: Example of Fourier transform of a source intensity.

One can see from both the expression for the convolution given above, as well as the plot of it in Fig. 3-4, that the window function introduces extra noise into the Fourier transform of the source signal. If we could remove the low frequency components of the source signal's Fourier transform by setting to zero all Fourier components with frequencies of absolute value less than or equal to $\nu_{\rm char}$, all that would be left in the source signal's Fourier transform would be the peak at frequency $\nu = 3$. The convolution of the window function with the source signal's Fourier transform with just this feature would be significantly less noisy, and one would be able to pick out easily candidate periods for a source. As it stands, one cannot easily interpret what feature in Fig. 3-4 represents a true signal. Note that, because any feature in a PDS has a finite frequency width, the convolution of the FT of a window function with that of a source intensity would result in both the shifting of the $\bar{s}(\nu)$ as well as smearing of its features, thus making the situation worse for data analysis.

Now we are in a position to explain why removing low-frequency source variability might lead to less noise in the PDS we calculate based on our data. Consider a source with strong red noise. In the convolution of the source's Fourier transform with the window function, for every value of ν for which there is a peak in the window function,

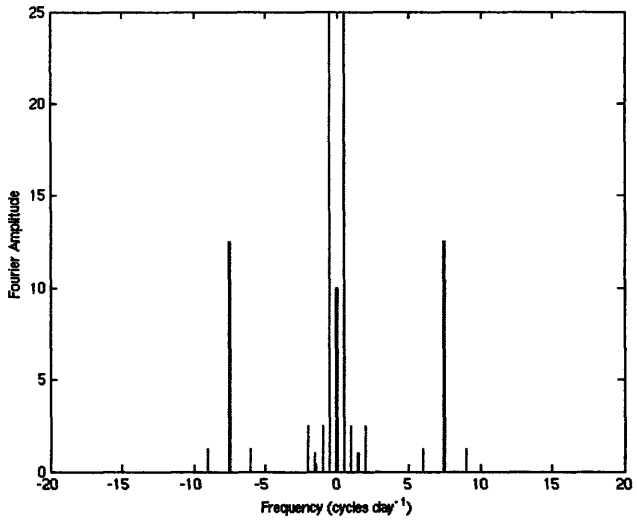

Figure 3-4: Convolution of $\bar{w}(\nu)$ and $\bar{s}(\nu)$.

the convolution integral evaluated at ν will tend to be very large, as both the artifact in the window function and the red-noise of the source tend to be very strong and they coincide in the convolution integral evaluated at ν, so the overlap is maximized. Furthermore, depending on the characteristic frequency width of the source's red-noise, the artifact in the window function may be "spread out" over that frequency width in the PDS obtained from the intensity we observe, $x[t_i]$. Therefore, any frequency range in the PDS of $x[t_i]$ that coincides with that of a spike in the window function PDS tends to be dominated by the contribution of the spike. The size of this region tends to be set by the parameters of the source's noise. So, depending on the noise parameters of the source, a source signal located in a region close to — or perhaps even far away from — the frequency of a peak in the Fourier transform of the window function may be washed out in the PDS we calculate. This is because the finite size of the peak in the window function will cause a speading out of the peak in the PDS we calculate due to the effects of the convolution. Were a source signal present in the vicinity of the noise induced by the spreading, the noise might dominate the signal. This seems to imply that if we could remove low frequency variability in the source, and so remove a dominant part of the red noise, the smearing effect of

the convolution on the spikes in the window function would be minimized. So also would the amplitude of the spikes representing artifacts from the window function be reduced. In this way, we would obtain a "cleaner" PDS, one more amenable to finding periodic signals from the source in the data. Since low frequency source variability potentially causes a lot of noise, we should seek to eliminate as much red noise as possible before transforming to the Fourier domain.

We have attempted just that. We try to eliminate red noise by applying the following simple method. Consider a time-series $x[t_i]$. We know that, upon calculating the PDS of $x[t_i]$, we will find noise attributable to low frequency source variability. Therefore, we attempt to "subtract out" low frequency components. To do this, first we set a characteristic timescale, say d days. We then rebin the lightcurve into $d/3$ day long bins, and we call the rebinned light-curve $x'[t_i]$. Then, we calculate a smoothed light curve. We do this by calculating the average of the intensities of the dwells in each $d/3$ day bin, weighted by the inverse of their variances, and then we assign to the bin the weighted average. Then, for each set of three newly rebinned timebins, $x'[t_i]$, $x'[t_{i+1}]$, $x'[t_{i+2}]$, we calculate an average of the intensities, again weighted by their variances, and then we assign the middle bin of the three consecutive $d/3$ day timebins that average value. We repeat this process until each $d/3$ day long timebin has been assigned such an average. To obtain a smoothed lightcurve, $y[t_i]$, from $x[t_i]$, for every time-bin of the original lightcurve during which the source was detected (i.e. for every i such that $w[t_i] = 1$), we assign the time-bin $y[t_i]$ the value $x'[t_i]$, i.e. the value of the rebinned lightcurve evaluated at time t_i. Then, we perform the bin-wise subtraction, $z[t_i] = x[t_i] - y[t_i]$, to obtain a lightcurve $z[t_i]$ which shares much of the power-spectral characteristics of $x[t_i]$ except that the lowest frequencies of $x[t_i]$ are not present in $z[t_i]$. Indeed, $z[t_i]$ should have no low-frequency variability!

Since the rebinned lightcurve $x'[t_i]$ captures the variability of the source on timescales longer than d days, any Fourier modes contained in the whole time series with period greater than d days would be potentially removed from the lightcurve after subtraction. The procedure could thus efficiently eliminate noise arising from source power at periods greater than d days. On the other hand, any true signal, like an eclipse

with period $2d$ days, would be subtracted out as well.

To demonstrate the results of smoothed-subtraction, we show in Fig. 3-5 the result of the process after this algorithm was applied to data from GX 9+9, the same source whose window function PDS and PDS of the source's lightcurve before applying the cleaning procedure were shown in Fig. 3-1. Note that the y-axis on the top plot

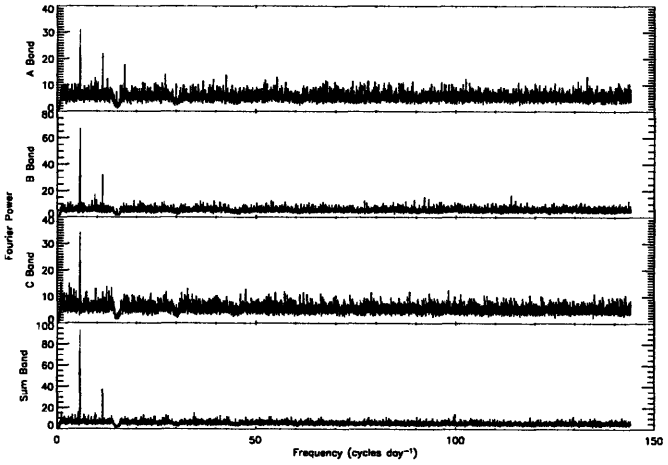

Figure 3-5: Power Density Spectra of GX 9+9 after smoothed-subtraction with a timescale of 1.0 days.

has been chosen so as to coincide with that of the bottom plot. Also note the slight improvement of the signal at $P = 4.19344$ hours over that of the PDS in Fig. 3-1.

One question is immediately raised by our procedure: what happens if a signal present in the data has a low frequency, on the order of that of the broadband source noise we wish to eliminate? The side effect of any method to reduce the red noise in a spectrum will be to reduce the significance of any periodic signal detected in the PDS. We might be able to mitigate this by focusing on the elimination of successively smaller bands of red noise, e.g. first from 0 to 0.2 cycles day^{-1}, then from 0 to 0.05 cycles day^{-1}, and so forth. In this way, a given signal might not be terribly degraded by using a method that reduced the noise in a small enough frequency range.

Now that we have discussed our procedure for "cleaning" the PDS, we must estab-

lish guidelines for determining whether any features of the PDS are either spurious or represent actual periodic modulation.

3.2 Statistical Analysis of Power Density Spectra

Given a power spectrum, we wish to calculate a significance threshold. That is to say, we wish to calculate a power level P at which the probability of a power exceeding P at any point in the spectrum by chance is less than a given (small) number, α. We assume that, outside of regions of strong artifacts such as at $1, 15, \ldots$ cycles day^{-1}, the spectrum is adequately represented by Gaussian white noise, which exhibits an exponential probability distribution. If the spectrum has been normalized such that $P[\nu_k]$ averages to 1, then the probability of finding that the power associated with one bin exceeds P_0 is given by:

$$\alpha(P > P_0) = e^{-P_0} \tag{3.6}$$

With this, we should be able to set any α and determine the power threshold P or greater such that a signal with power P has probability α to occur by chance.

In what follows, all Fourier transforms are calculated with 4478976 points. This is the number of points because of our procedure to calculate the FFT of the data set. We have rebinned the original data set into 5 minute time bins. For efficiency purposes, we calculated a number near to the number of 5 minute time bins that was the product of small primes. This number was then multiplied by a factor of 4 because we wanted to pad the data set with zeroes to get higher frequency resolution. The number above was the result of these calculations.

We consider the two general searches — the one for periodicities and the one for time-variable modulation — separately. For each search, there are 443 sources in the ASM catalog. We also compute 4 spectra: one for each energy band and the sum band (1.5-12 keV). In each PDS, only half of the frequencies are independent because the Fourier transform of a real time-series results in the same power at ν_k

and $-\nu_k$, so we only count half of them in the significance analysis. We require that a significant power level should only be observed on average once in the entire search for periodicities. The probability of observing a power P_0 in a given bin in the PDS for a particular timescale is given by

$$(2239488 * 443 * 4)^{-1} = e^{-P_0} \tag{3.7}$$

$$\rightarrow P_0 = 22.1. \tag{3.8}$$

Therefore, if any bin in our search for modulation that is not associated with a previously observed periodicity has associated with it a power higher than ~ 23, we will associate that frequency with a significant periodicity. If the periodicity has been observed before, our power threshold will be somewhat lower.

For the time-variable search, we will divide the lightcurves into three equal pieces, and we assume that the statistics of the PDS do not vary much among the pieces for a given source. Therefore, we calculate that the threshold for detection in the time-variable search using a given smoothing timescale is given by:

$$(2239488 * 443 * 4 * 3)^{-1} = e^{-P_0} \tag{3.9}$$

$$\rightarrow P_0 = 23.18 \tag{3.10}$$

So if a source has a Fourier power in our time-variable modulation search that is ~ 24 or above, we will associate it with a significant periodicity. Similarly to the case mentioned above, if a periodicity has been previously observed, a lower power threshold is required to call it significant.

We note that there are problems with this approach. Among the most obvious is that there is no guarantee that the PDS of a given source after smoothing is characterized by Gaussian white noise (GWN) even if the PDS is characterized by GWN, as is the assumption in the calculations above. This is borne out by the fact that, for smoothing time-scales on order of $0.3 - 1$ day, one sees "dips" in the power spectra located where the artifacts in the power spectra of the window functions are.

These certainly cannot be characterized by GWN. However, outside of these regions, the assumption that the PDS statistics behave like those of GWN is probably an okay first order approximation to the underlying noise distribution.

3.3 Previous Searches

There have been three general searches for periodicities in RXTE ASM data of which the author is aware. The first such search was conducted by Linqing Wen *et al.* (2006). They applied a Lomb-Scargle periodiogram analysis, a variant of the Fourier analysis we employ, to conduct their search.

The second such search was carried out by Shivamoggi (2005). Therein, she used a technique in which she applied standard Fourier techniques and a whitening algorithm to divide the power at each point in the PDS by a local average of the power near that point, because artifacts tend to be more "spread out" in the Fourier domain than true source signals. Most notable in this work was her discovery of the 4.2 hour periodicity in the Galactic bulge source GX 9+9, a periodicity that had been previously found, but not in ASM data.

Levine and Corbet (2006) conducted a general search using the smoothing and subtraction method described in Section 3.1, and they found $\sim$10 periodicities previously unobserved in ASM data.

In this present work, we apply the same method Levine and Corbet used to conduct both (a) a general search of ASM data for periodicities, and, (b) a general search for time-variable modulation strength in sources.

Chapter 4

Results of General Periodicity Search in RXTE ASM Data

In this chapter, we present the results of a general periodicity search of RXTE ASM data using the smoothing-subtraction method described in the previous chapter. We employ this method in a Fourier analysis of the ASM light curves of 443 sources in the ASM catalog that represent data until week 531 of the mission (approximately March 2006). The last year of data was not available as of April, 2007, because a major effort at correcting all the data for degradation of the SSCs had only been completed for data up to that point, so we could not include the last year of data in our analysis.

Below, we present the findings by order of type of object, if known. We also discuss the systems and give a limited account of past research that has been conducted into their nature. Our results are succinctly given in Appendix 1.

4.1 High Mass X-ray Binaries

Centaurus X-3 (also called 4U 1118-60) is a dipping and eclipsing SG/HMXB with a pulsar companion located in the constellation Centaurus. Approximately 10 ± 1 kpc away from the Sun, it resides in the Galactic plane (Hutchings *et al.*, 1979).

The orbital period of the binary was first reported by Schreier *et al.* (1972b) to be 2.08712 ± 0.00004 days on the basis of *Uhuru* data. It notably was also the first X-ray pulsar to be discovered, exhibiting a pulse period of $P_{\rm pulse} = 4.84$ sec, as reported in Giacconi *et al.* (1971). The strongest detection in our Fourier analysis indicates a strong modulation in all bands at a period of $P = 2.0870 \pm 0.0006$ days, which is consisent with the orbital period found by Schreier *et al.*

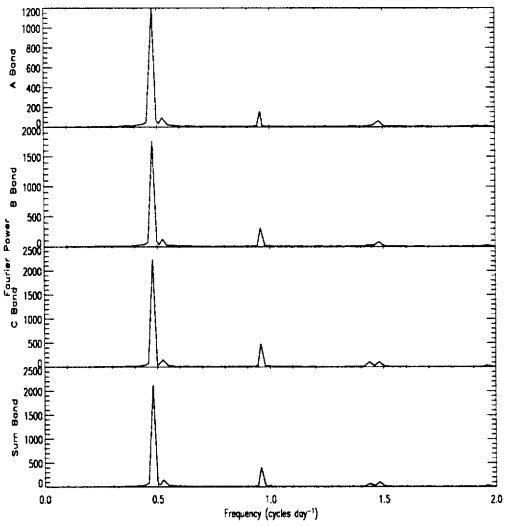

Figure 4-1: Power density spectrum of Cen X-3

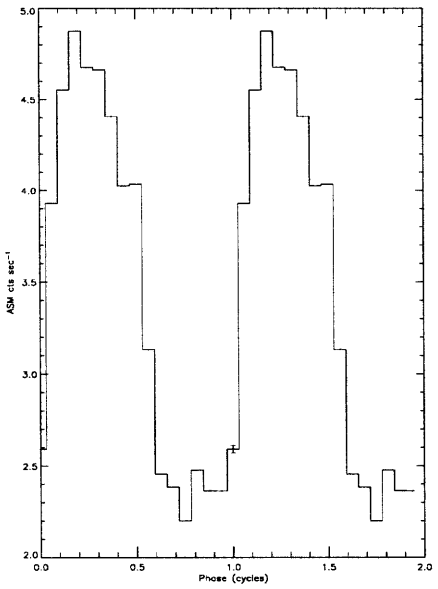

Figure 4-2: Folded lightcurve of Cen X-3

Cygnus X-1 is a dipping HMXB located in the constellation Cygnus that houses a $14 \pm 2\ M_{\odot}$ black hole candidate (BHC) (Kubota, 1998). Holt *et al.* (1976) reported the detection of the orbital period, $P \sim 5.6$ days, in this system using data from *Ariel V*. State transitions are seemingly important in this source, with, e.g., Wen *et al.* (2006) reporting that when Cyg X-1 is in the low/hard state (low 2-10 keV luminosity with a fairly hard spectrum), the orbital period of $P = 5.6008 \pm 0.0007$ days is observed, but the orbital period is not observed when Cyg X-1 is in the high/soft state. We report a period in all bands found to be 5.601613 ± 0.16 days, and this period is consistent with the orbital period of the source.

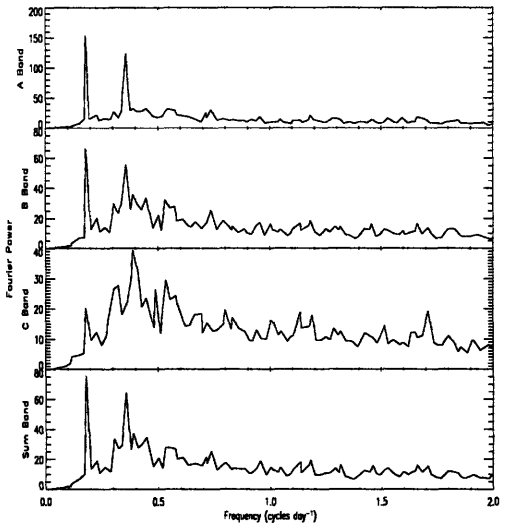

Figure 4-3: Power density spectrum of Cyg X-1

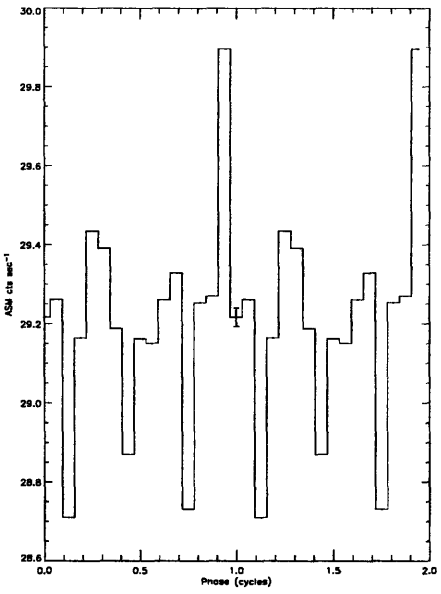

Figure 4-4: Folded lightcurve of Cyg X-1

Cygnus X-3 is a Be/HMXB system located in the constellation Cygnus. The exact nature of its compact object is not known. Lommen *et al.* (2005) suggested two models of Cyg X-3 consistent with observations: a system in which a black hole accretes from a 7 $M_{\odot}$ Wolf-Rayet (WR) star and one in which a neutron star accretes from a $1.5M_{\odot}$ helium star. van Kerkwijk *et al.* (1996) found that the source's I and K band spectra show emission lines characteristic of a subclass of WR stars. The spectra, combined with van Kerkwijk *et al.*'s simple model of the source that matches observations, caused them to conclude that Cyg X-3 does indeed contain a WR star. We detect an X-ray period in all bands at $P = 4.79256 \pm 0.00012$ hours. This period is consistent with that first reported by Parsignault *et al.* (1972) using data from the *Uhuru* satellite. Wen *et al.* (2006) also report a periodicity based on RXTE ASM data that is consistent with our period.

IGR J1914+0951 was discovered by Hannikainen *et al.* (2003) on the basis of *INTEGRAL* data. Corbet *et al.* (2004) found a 13.55 day periodicity in the ASM light curve over the first three years of the mission, but not during the subsequent years.

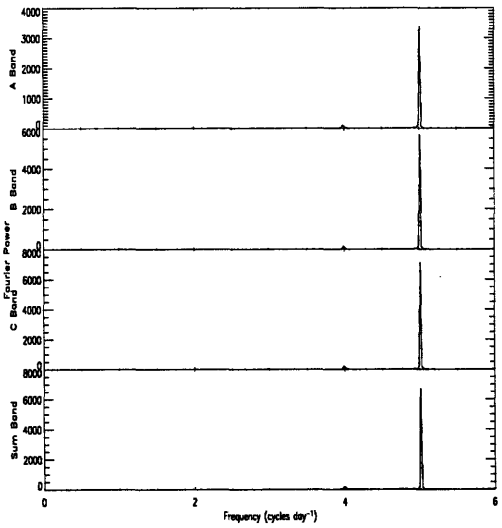

Figure 4-5: Power density spectrum of Cyg X-3

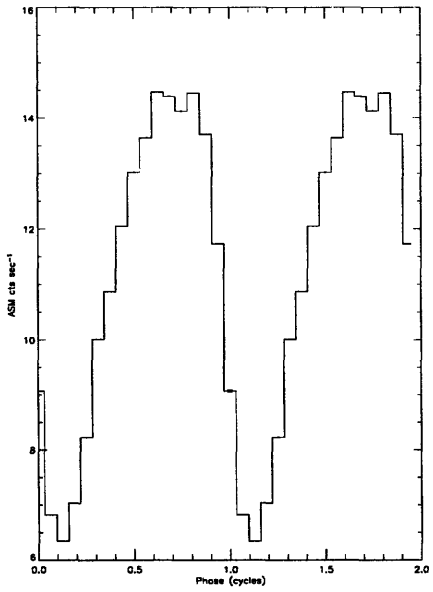

Figure 4-6: Folded lightcurve of Cyg X-3

Wen *et al.* (2006) found this periodicity in their search to be at 13.552±0.003 days. We have found it most strongly in the C band, and we detect it to be $P = 13.5318 \pm 0.004$ days.

LMC X-4 is a neutron star-containing HMXB located in the Large Magellanic Cloud. The neutron star is also a pulsar with pulse period $P_{\rm pulse} \sim 13.5$ seconds (Kelley *et al.*, 1983). The orbital period of LMC X-4 was inferred to be 1.408 ± 0.002 days from optical observations of a candidate for its counterpart by Chevalier and Ilovaisky (1977). It was found to have an X-ray period of ~ 30.5 days by Lang *et al.* (1981), and they interpreted the periodicity as a superorbital period in the binary owing to blockage of X-rays from the central source by a precessing accretion disk. Wen *et al.* (2006) detected both the orbital period and the superorbital period in RXTE ASM data. We detect strongly both the orbital period at $P = 1.4080 \pm 0.0003$ days and its first two harmonics in all bands except for the A band.

RX J0037.2+6121 (= IGR J00370+6122) is a SG/HMXB discovered in 2004 by den Hartog *et al.* (2004) using data from the *INTEGRAL* satellite. An X-ray

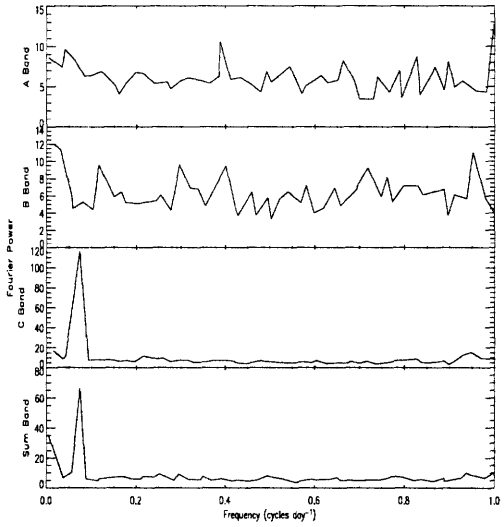

Figure 4-7: Power density spectrum of IGR J1914+0951

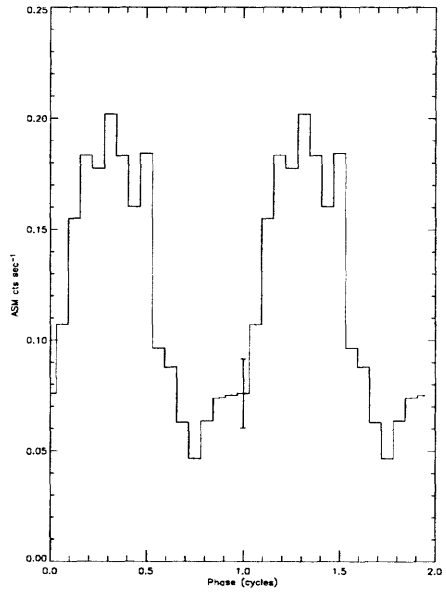

Figure 4-8: Folded lightcurve of IGR J1914+0951

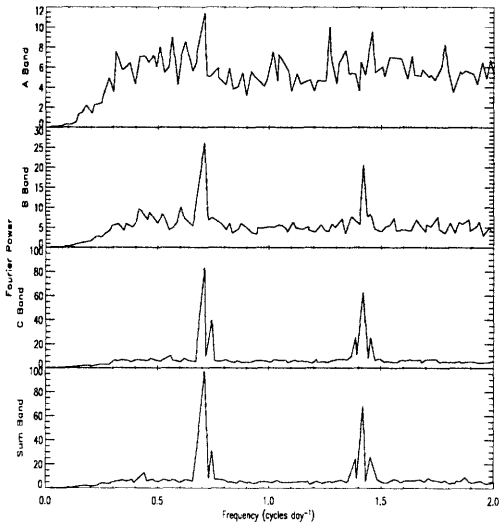

Figure 4-9: Power density spectrum of LMC X-4

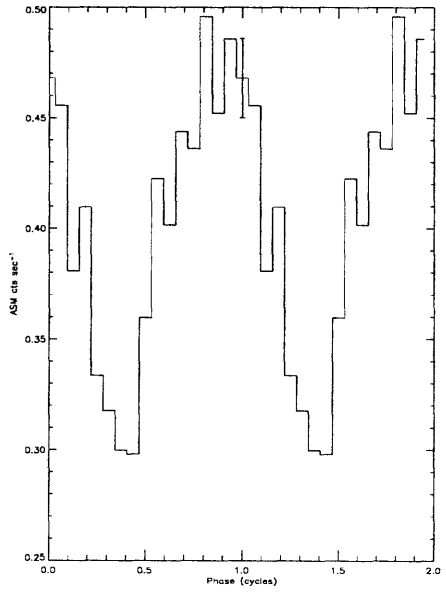

Figure 4-10: Folded lightcurve of LMC X-4

period of 15.665 ± 0.006 days was found using RXTE ASM data by den Hartog *et al.* and is identified as the orbital period. We report a detection of a 17.24453 ± 0.00003 min periodicity in the A band ASM data. The power associated with the frequency bin corresponding to this period has probability 4.8% to be seen in the entire search, so we regard the detection as significant. The nature of the compact object is not certain, but if it is a neutron star, it is possible that this is a harmonic of its spin period.

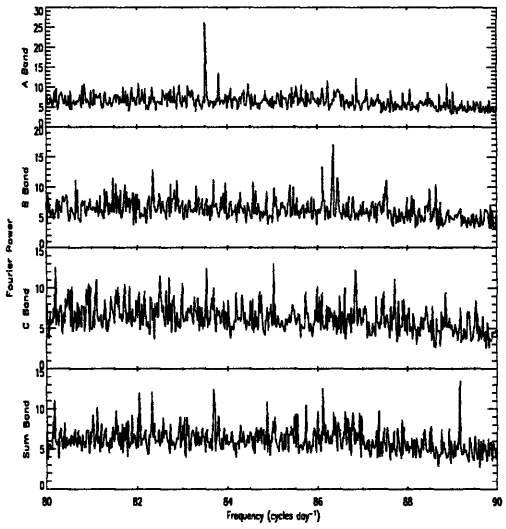

Figure 4-11: Power density spectrum of RX J0037.2+6121

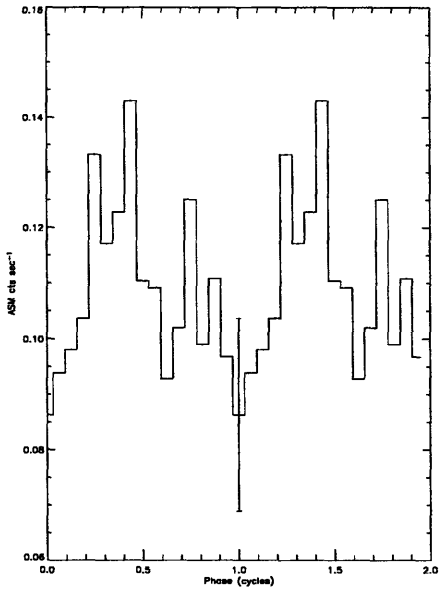

Figure 4-12: Folded lightcurve of RX J0037.2+6121

SAX J2103.5+4545 is a Be/HMXB transient system that was discovered during its 1997 outburst by the *BeppoSAX* satellite (Hulleman *et al.*, 1998). During the outburst, it was discovered to have coherent pulsations with $P_{\rm pulse} = 358.61$ sec which indicated the compact object to be a neutron star. ASM observations of the source analyzed by Baykal *et al.* (2000) indicated that the system has an orbital period of 12.68 days, and this result was corroborated by results from Wen *et al.* (2006) which give a period of 12.673 ± 0.004 days. We also detect this period to be at $P = 12.82 \pm 0.1$ days in all bands except for the A band.

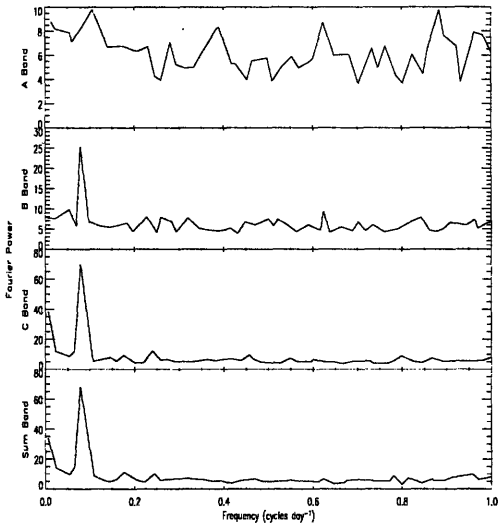

Figure 4-13: Power density spectrum of SAX J2103.5+4545

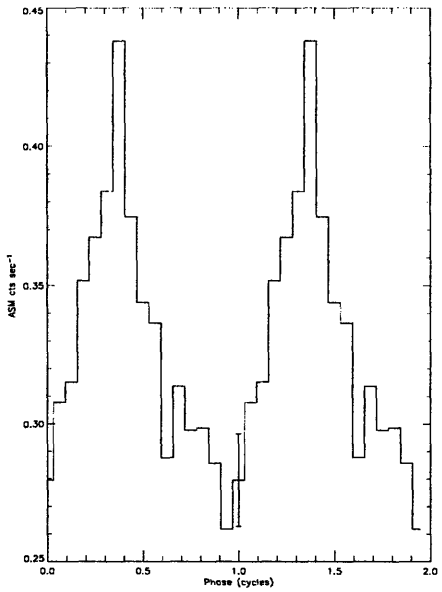

Figure 4-14: Folded lightcurve of SAX J2103.5+4545

SMC X-1 is a neutron star-containing SG/HMXB system that undergoes eclipses and which is located in the Small Magellanic Cloud. Its neutron star is a pulsar observed by Lucke *et al.* (1975) to have a pulsation period $P_{\text{pulse}} = 0.71$ sec. This system was found to have an orbital period of 3.89 days by Schreier *et al.* (1972a). Wen *et al.* (2006) also detect this periodicity. We detect the period extremely strongly in all bands at $P = 3.893 \pm 0.002$ days, and its harmonics are also detected extremely strongly.

SS 433 is a binary system thought to contain a black hole that is a prominent jet source. The jets have been observed to precess on a cone of half-angle $\theta = 20°$ with a precession period of 162 days. The orbital period of the binary system was found to be 13.1 days by Crampton *et al.* (1980). Gies *et al.* (2002) found this period in the RXTE ASM data to be 13.075 ± 0.017 days. It is detected most notably in the C band. We have found it to be $P = 13.1233 \pm 0.01$ days.

X0114+650 is a SG/HMXB system containing a pulsar. Periodic outbursts with $P = 2.78$ hours were first discovered on the basis of combined *EXOSAT* and *ROSAT*

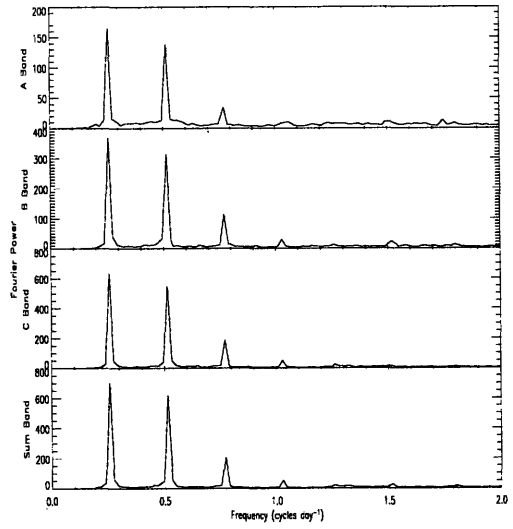

Figure 4-15: Power density spectrum of SMC X-1

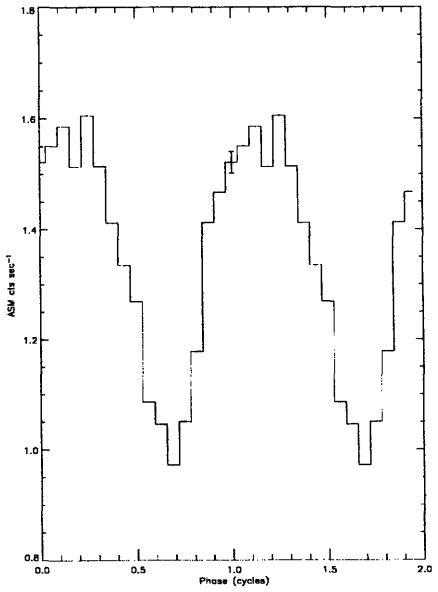

Figure 4-16: Folded lightcurve of SMC X-1

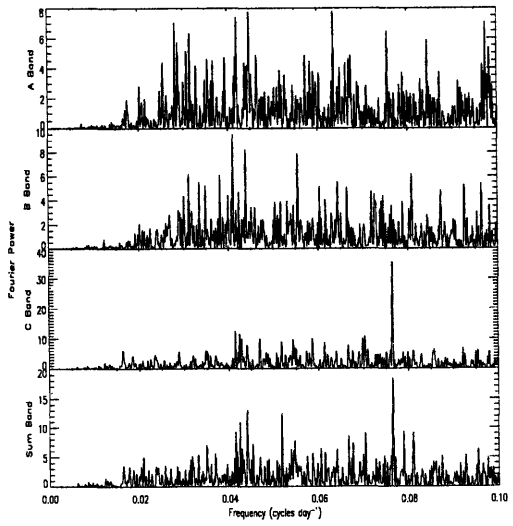

Figure 4-17: Power density spectrum of SS 433

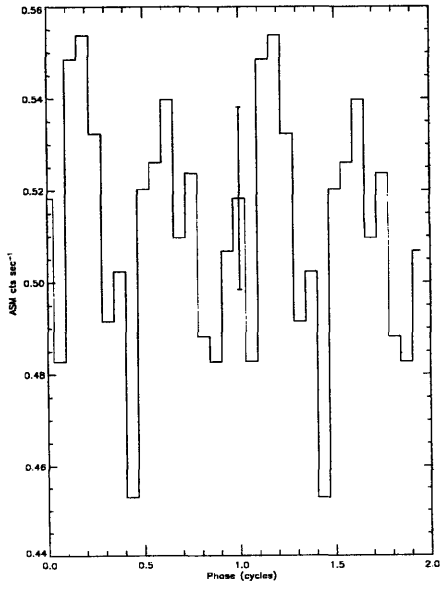

Figure 4-18: Folded lightcurve of SS 433

data by Finley *et al.* (1992); these outbursts were later shown to be pulsations from the neutron star in the system by Corbet *et al.* (1999). Crampton *et al.* (1985) first found the orbital period of the system to be 11.59 days on the basis of optical measurements, and Corbet *et al.* (1999) found this modulation in X-rays using ASM data. Wen *et al.* (2006) find both periodicties, at 2.7421 ± 0.002 hrs and 11.599 ± 0.005 days, repectively. We detect the orbital period at $P = 11.5985 \pm 0.02$ days in the sum band.

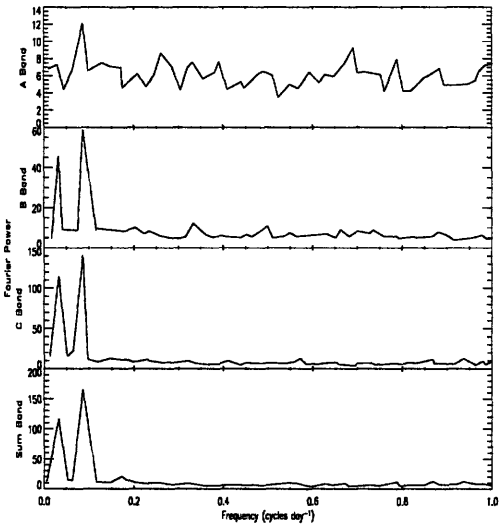

Figure 4-19: Power density spectrum of X0114+650

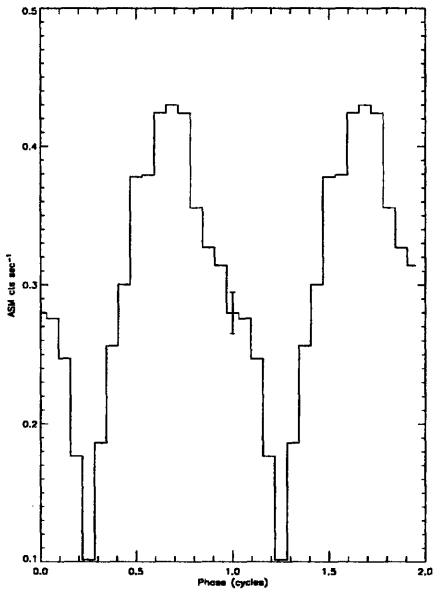

Figure 4-20: Folded lightcurve of X0114+650

X1538-522 is an eclipsing neutron star-containing HMXB. The neutron star is a pulsar with a pulsation period discovered independently by groups working with *Ariel V* and *OSO-8* data to be 529 sec in 1977 (see e.g. Davison *et al.* (1977) and references therein). In addition to the pulse period observed by the *OSO-8* group, they found clear evidence of orbital modulation at $\sim$ 3.75 days. Wen *et al.* (2006) also found this periodicity in RXTE ASM data to be 3.7284 ± 0.0003 days. We find a strong signal at $P = 3.72856 \pm 0.07$ days in all bands.

X1657-415 is an eclipsing SG/HMXB housing a pulsar whose pulse period was

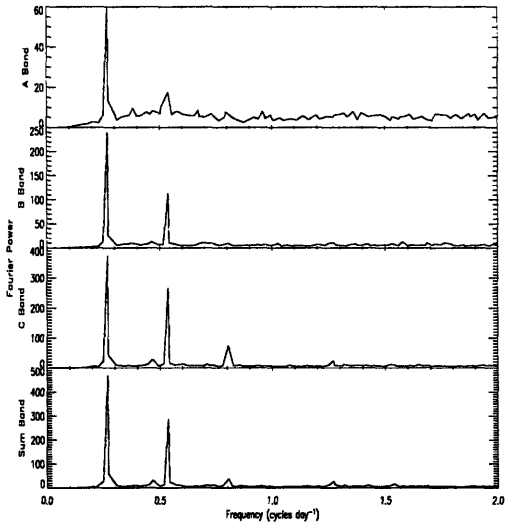

Figure 4-21: Power density spectrum of X1538-522

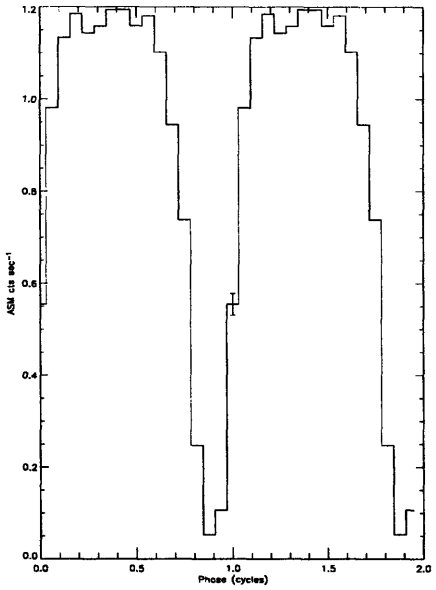

Figure 4-22: Folded lightcurve of X1538-522

determined to be 38.22 sec in *HEAO 1* observations by White and Pravdo (1979). The discovery of both the orbital parameters of the system and the supergiant nature of the companion is due to Chakrabarty *et al.* (1993) who found an orbital period of 10.4436 ± 0.0038 days using *BATSE* data. Wen *et al.* (2006) found a refined orbital period of 10.4462 ± 0.0002 days. We confirm this with a period of $P = 10.44932 \pm 0.005$ days from a detection of the period's first harmonic. The signal was most strongly detected in the C band.

X1700-377 is a neutron star-containing SG/HMXB whose X-ray spectrum is similar to those of X-ray pulsars (Gottwald et al 1986), but from which no coherent pulsations have been yet observed. Its orbital period was detected by Jones *et al.* (1973) in *Uhuru* data to be 3.412 ± 0.002 days. Subsequent X-ray results from the RXTE ASM yielded an X-ray period consistent with this result, with Wen *et al.* (2006) reporting 3.4117 ± 0.0002 days. We have found evidence of a $P = 3.411 \pm 0.002$ day period in all bands.

X1907+097 is a pulsar-containing SG/HMXB system powered by wind accretion

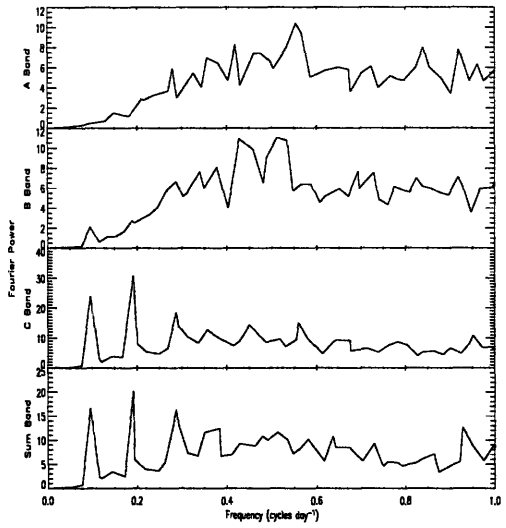

Figure 4-23: Power density spectrum of X1657-415

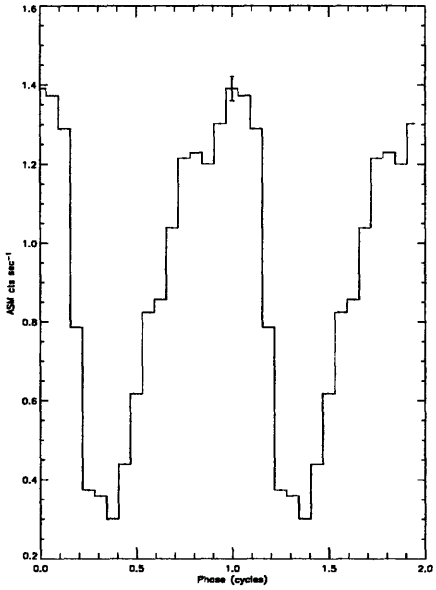

Figure 4-24: Folded lightcurve of X1657-415

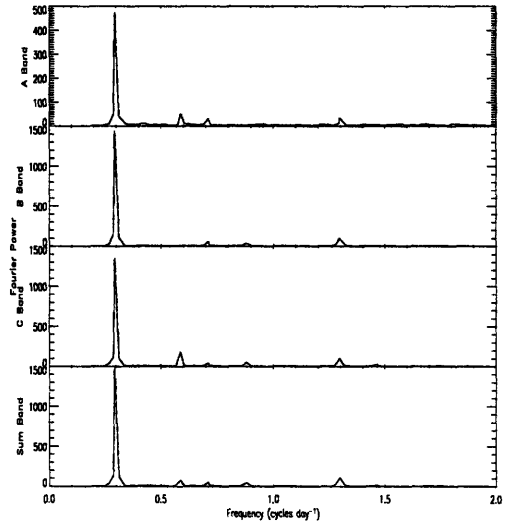

Figure 4-25: Power density spectrum of X1700-377

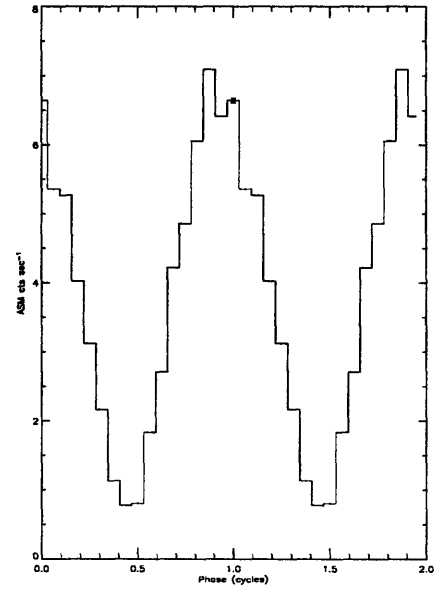

Figure 4-26: Folded lightcurve of X1700-377

from the supergiant companion. Its orbital period of 8.38 days was first discovered on the basis of *Ariel V* data by Marshall and Ricketts (1980), and its pulse period of $P_{\rm pulse} = 437.5$ sec was first discovered by Makishima *et al.* (1984) on the basis of *Tenma* data. The orbital period was found in ASM data by Wen *et al.* (2006) in their periodicity search in 2005 to be 8.375 ± 0.002 days. We have found the period to be $P = 8.3682 \pm 0.003$ days, as detected in the sum band.

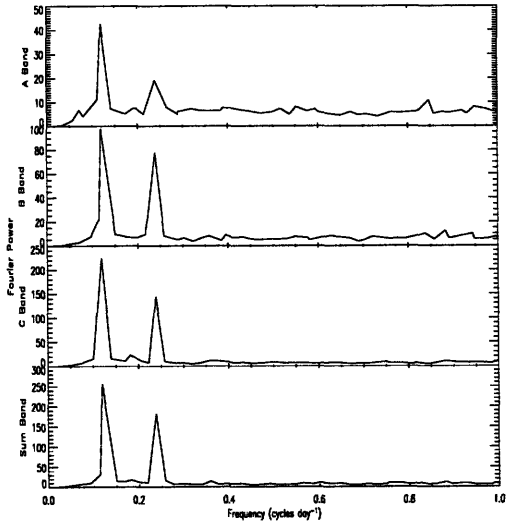

Figure 4-27: Power density spectrum of X1907+097

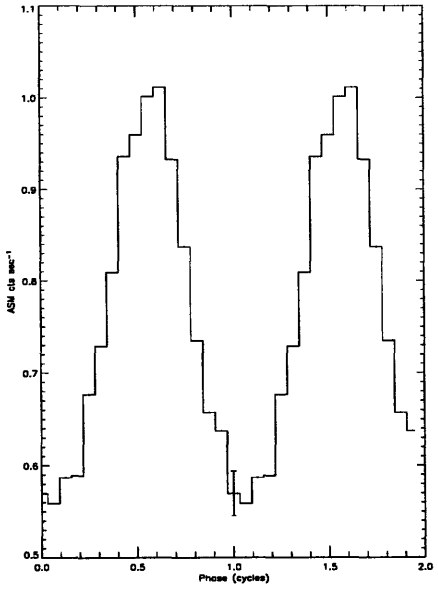

Figure 4-28: Folded lightcurve of X1907+097

X1908+075 is a SG/HMXB system housing a pulsar as the compact object whose pulse period, 605 sec, was discovered by Levine *et al.* (2004) on the basis of RXTE PCA data. Wen *et al.* (2000) find a 4.4 hr periodicity in ASM data, and the detection is also present in the subsequent analysis of ASM data by Wen *et al.* (2006). We detect a period of $P = 4.3985 \pm 0.0005$ days in the sum band.

XTE J1855-026 is a neutron star-containing SG/HMXB system which was discovered by the RXTE PCA in 1998 during scans along the Galactic plane (Marshall and Takeshima, 1998). The neutron star shows pulsations at approximately 361 sec, but this pulsation period was not detected in our analysis of the ASM data. The

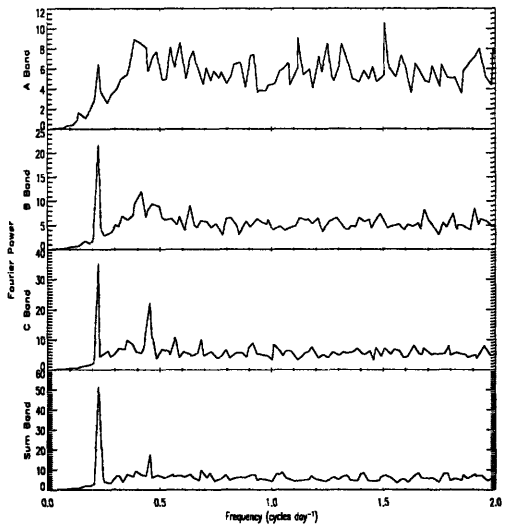

Figure 4-29: Power density spectrum of X1908+075

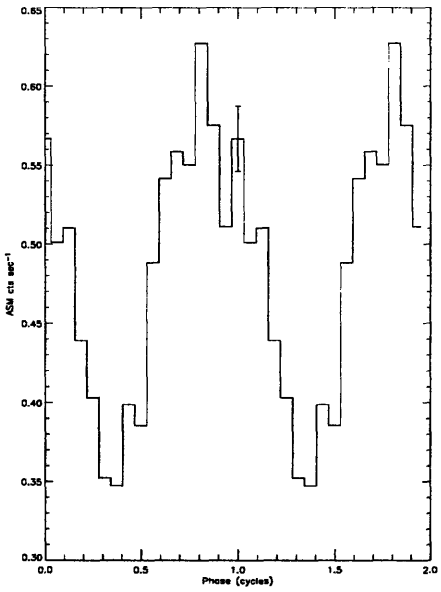

Figure 4-30: Folded lightcurve of X1908+075

orbital period was discovered by Corbet (1998) to be 6.074 ± 0.004 days on the basis of RXTE ASM data using the frequency of the best fit sine-wave to determine the period. Wen *et al.* (2006) found this period to be $P = 6.0752 \pm 0.0008$ days. We have determined a period of 6.071645 ± 0.005 days from the harmonic as detected in the C band. This period determination is consistent with both earlier results.

X Persei (= X0352+30) is a Be/HMXB system with a neutron star that was shown to exhibit pulsations at 837 seconds by White *et al.* (1976). The orbital period of the system was shown to be 250 days by Delgado-Martí *et al.* (2001). Wen *et al.* (2006) did not detect this periodicity strongly, though they consider it a detection because it was previously known. We report a detection of the pulse period at $P = 837.7928 \pm 0.001$ sec in the sum band.

4.2 Low Mass X-ray Binaries

EXO 0748-676 is a LMXB containing a neutron star; its eclipse and dipping events are both visible in X-rays. The orbital period of the source is found to be $3.8241 \pm$

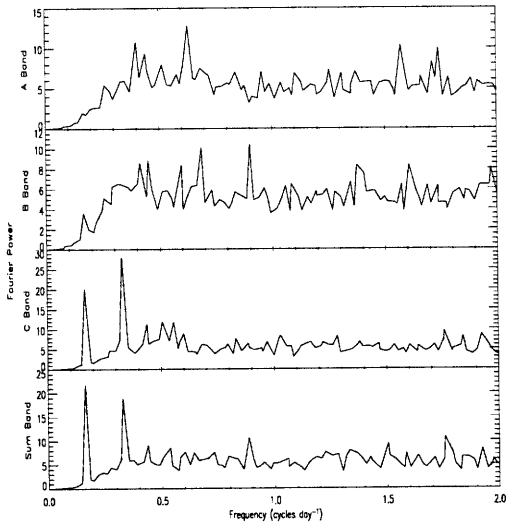

Figure 4-31: Power density spectrum of XTE J1855-026

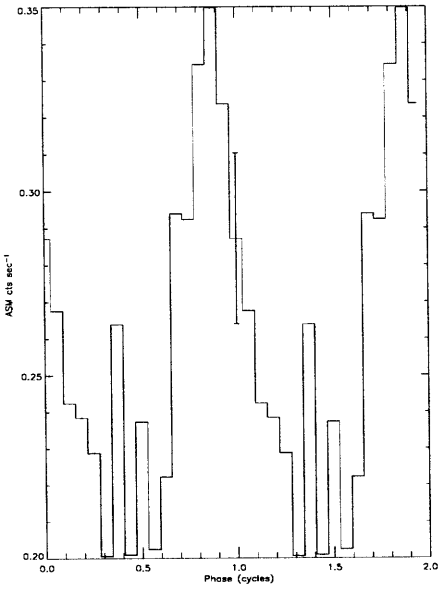

Figure 4-32: Folded lightcurve of XTE J1855-026

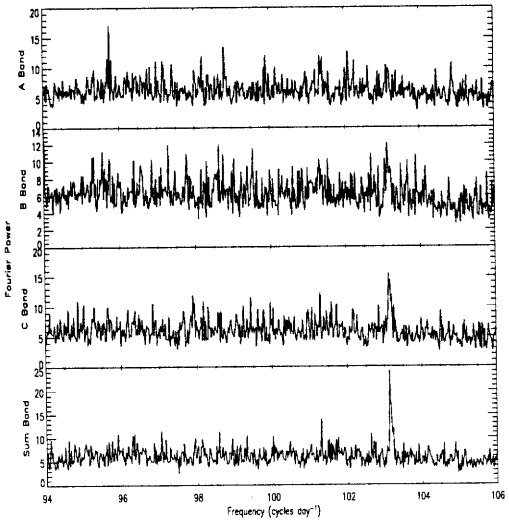

Figure 4-33: Power density spectrum of X Per

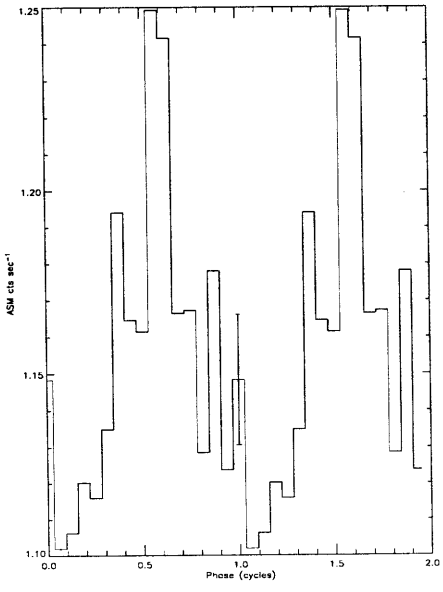

Figure 4-34: Folded lightcurve of X Per

0.0008 hrs, and the eclipse lasts approximately 500 seconds. We detect the period in the B and sum bands. Judging by the fact that an eclipse is observed, the system must be viewed at a very high inclination angle. This period was first discovered by Parmar *et al.* (1985).

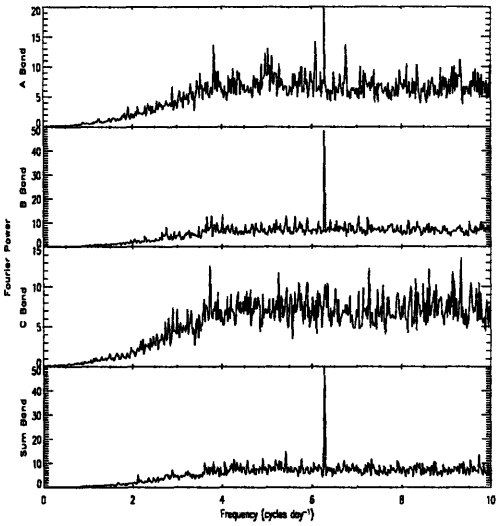

Figure 4-35: Power density spectrum of EXO 0748-676

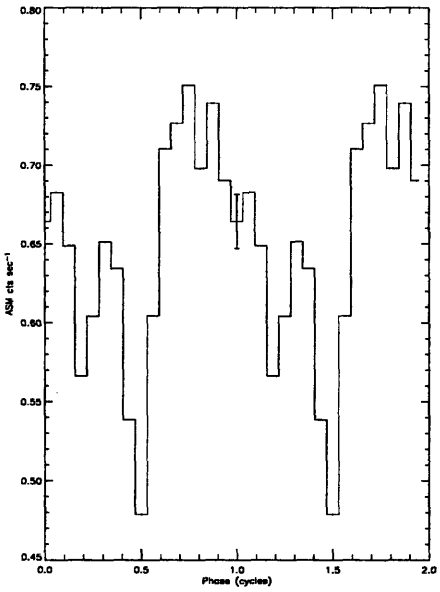

Figure 4-36: Folded lightcurve of EXO 0748-676

GRO J1655-40 is a LMXB transient X-ray source that houses a black hole candidate. It recently — during 2005 — underwent an outburst. Bailyn *et al.* (1995) established from radial velocity measurements of the companion star that the optical period was 2.601 ± 0.027 days. Levine and Corbet (2006) find a period in X-rays of 2.627 ± 0.007 days using ASM data. We confirm their result with our detection of a periodicity at $P = 2.6219 \pm 0.005$ days in all bands.

GX 9+9 is a atoll LMXB containing a neutron star, the orbital period of which was first discovered by Hertz and Wood (1988) on the basis of *HEAO 1* data. They fit a sinusoid to the data and found the best-fit period to be 4.19 ± 0.02 hours with a $\sim 3.8\%$ amplitude, which they interpreted as the orbital period of the binary system. Schaefer (1990a) observed this period in the optical via V, B, and R

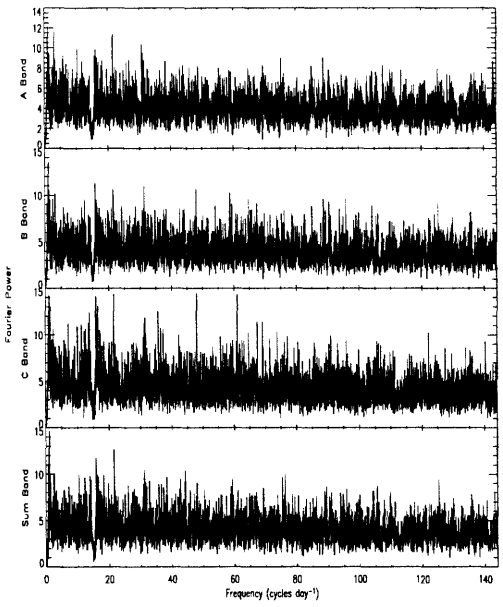

Figure 4-37: Power density spectrum of GRO J1655-40

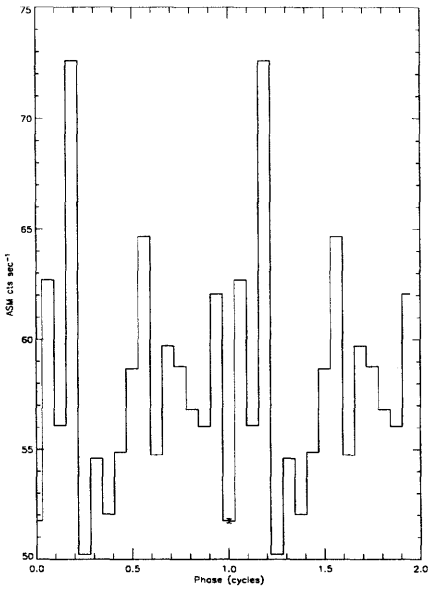

Figure 4-38: Folded lightcurve of GRO J1655-40

band measurements. We detect their periodicity very significantly in all bands to be $P = 4.19342 \pm 0.000095$ hrs. This source will be discussed at length in the next chapter, as the source experiences sharp changes in the strength of its modulation.

Hercules X-1 is an eclipsing LMXB containing a pulsar. Discovered in 1972, the pulse period was determined to be 1.24 seconds on the basis of *Uhuru* data, the the orbital period was found to be 1.7 days Tananbaum *et al.* (1972). Soon afterwards, a superorbital period of $\sim$ 30 days was discovered. This source was detected in the periodicity search of Wen *et al.* (2006). We also find this periodicity at $P = 1.7001 \pm 0.0003$ days.

X1254-690 is a dipping LMXB which is a Z source containing a neutron star. It was first identified as an X-ray dipper Courvoisier *et al.* (1986), who found very deep dipping (up to 95% of the non-dipping intensity) during *EXOSAT* observations of the source. The period of these dips was determined to be 3.88 ± 0.15 hours. We find a signal in the sum band that is consistent with both those results and the results of Levine and Corbet (2006). Our period is determined to be $P = 3.93333 \pm 0.00008$

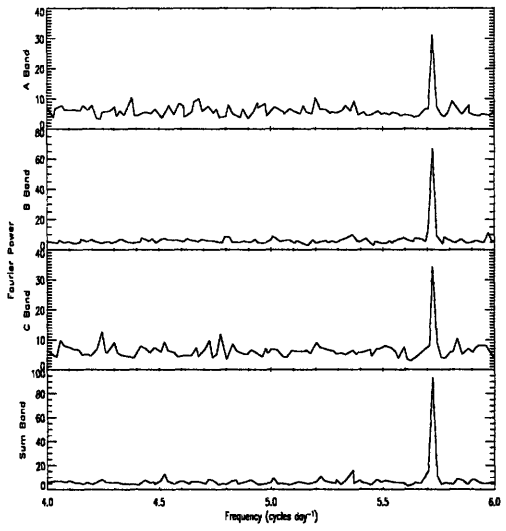

Figure 4-39: Power density spectrum of GX 9+9

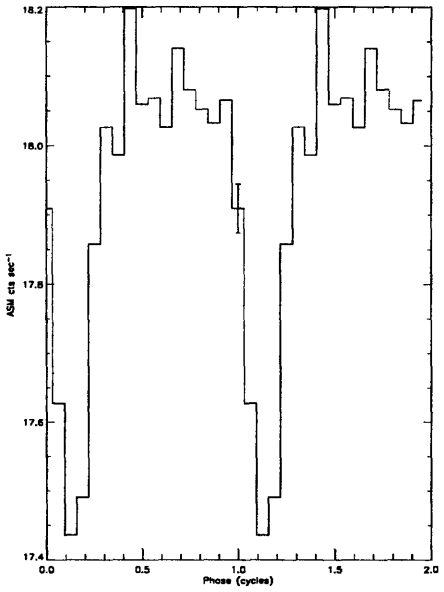

Figure 4-40: Folded lightcurve of GX 9+9

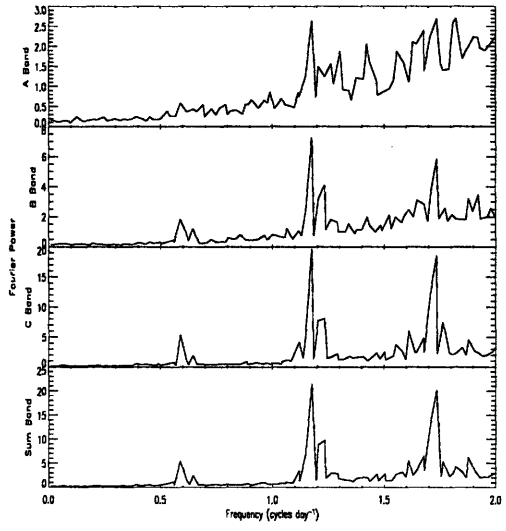

Figure 4-41: Power density spectrum of Hercules X-1

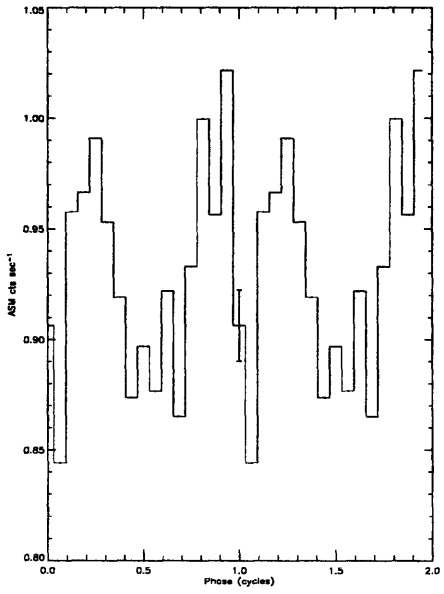

Figure 4-42: Folded lightcurve of Hercules X-1

hours.

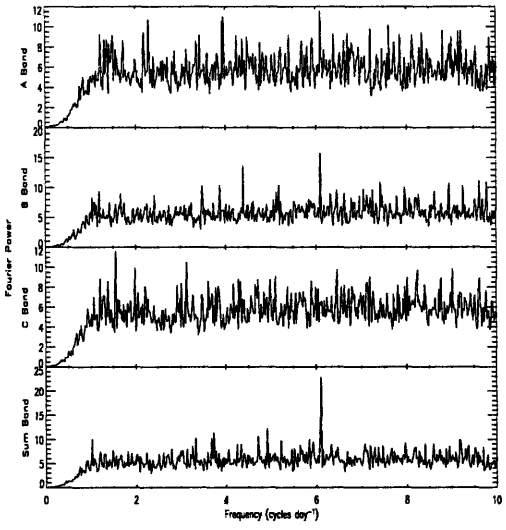

Figure 4-43: Power density spectrum of X1254-690

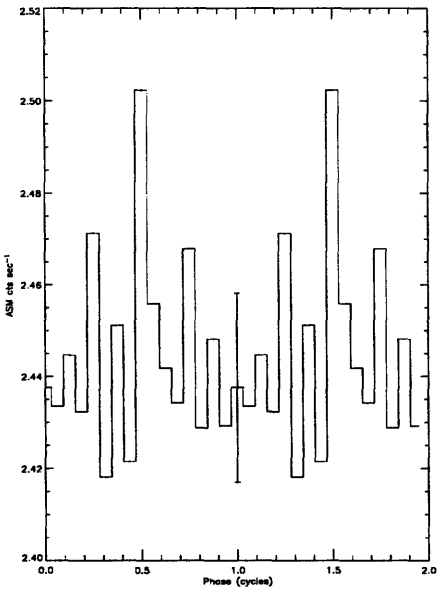

Figure 4-44: Folded lightcurve of X1254-690

X1323-619 is a NS containing LMXB dipping and bursting source. The periodic nature of the 50 minute long dips was first discovered by Parmar *et al.* (1989) on the basis of *EXOSAT* data. They found a period of approximately 2.932 ± 0.005 hours, with type-1 X-ray bursts occuring on average every 5.56 hours during their observation. This period was also found by Levine and Corbet (2006) to be 2.94192 ± 0.00004 hrs. We determine a period of $P = 2.94192 \pm 0.00005$ hours in the sum band. We do not observe any signature of periodic bursting in our data.

X1624-490 (= 4U 1624-490) is a dipping LMXB affectionately known as the "Big Dipper." It is an atoll source whose timing properties seem reminiscent of other atoll sources in the so-called "upper banana state." The source undergoes strong dipping (up to about 75% of its non-dipping intensity) with a period that was first discovered by Watson *et al.* (1985) to be 21 ± 2 hours from *EXOSAT* observations. RXTE ASM observations analyzed by Wen *et al.* (2006) also show the periodic dipping. We have detected this period in all bands except for the A band, but we detect more

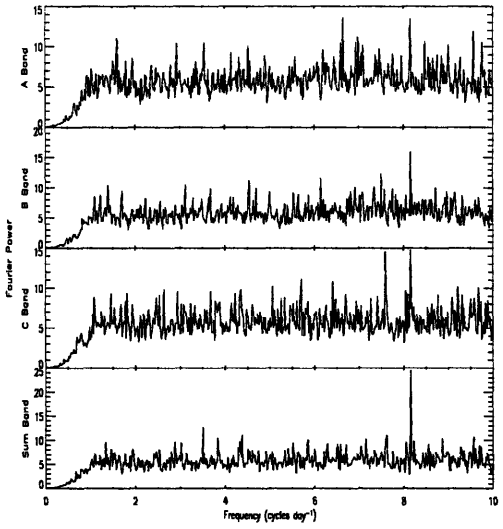

Figure 4-45: Power density spectrum of X1323-619

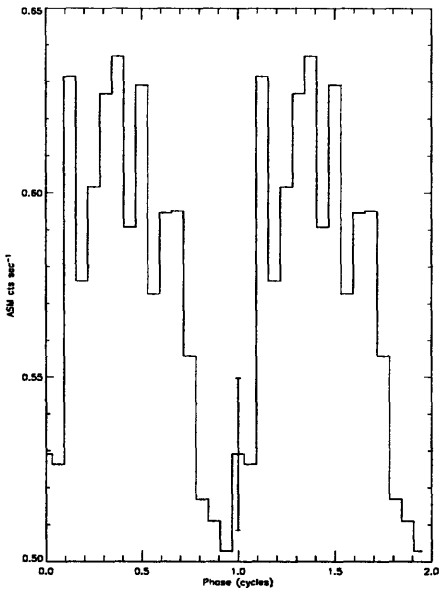

Figure 4-46: Folded lightcurve of X1323-619

strongly its first harmonic. As determined from the harmonic, we derive a period of $P = 20.8776 \pm 0.001$ hours.

X1658-298 is a transient bursting X-ray source discovered in 1976 by *SAS-3*. Using data from both *HEAO-1* and *SAS-3*, Cominsky and Wood (1984) were able to derive a 7.11 hour periodicity in the lightcurve which exhibited both dipping and eclipse events. From 1991 until 1999, the source was quiescent, but it turned on again in 1999. Wachter *et al.* (2000) made the first detection of the 7.11 hour orbital period in RXTE PCA data, and Wen *et al.* (2006) found the period in their search of ASM data. We detect the period in all bands to be at $P = 7.115749 \pm 0.01$ hours.

X1746-371 is an X-ray bursting and dipping source that is an LMXB located in the globular cluster NGC 6441. On the basis of *Ginga* observations, Sansom *et al.* (1993) reported a new period of 5.73 ± 0.15 hours. However, this new period is now believed to have been spuriously detected. Bałucińska-Church *et al.* (2004) found periodic dips with period $P = 5.16 \pm 0.01$ hours after an analysis of RXTE PCA data, and Levine and Corbet (2006) confirmed this periodicity using ASM data. Levine

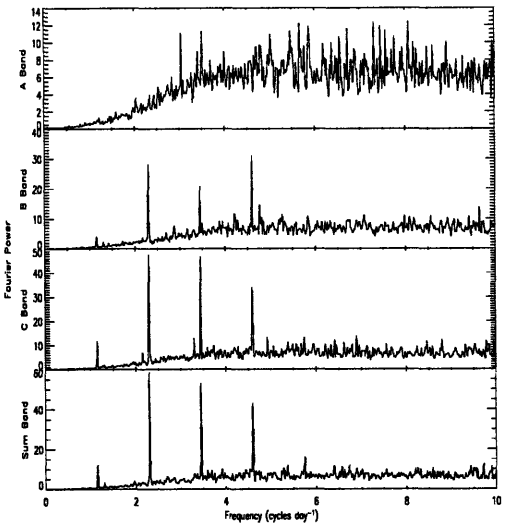

Figure 4-47: Power density spectrum of X1624-490

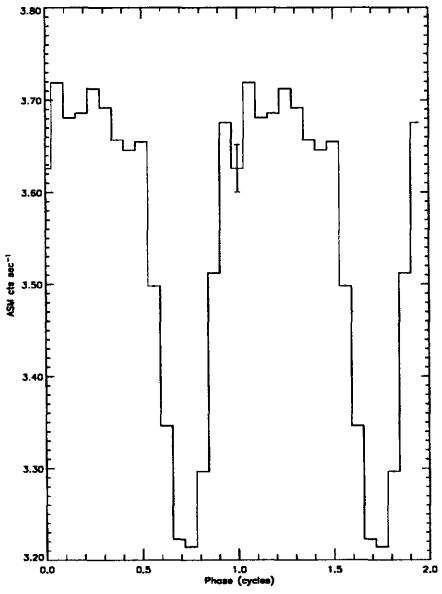

Figure 4-48: Folded lightcurve of X1624-490

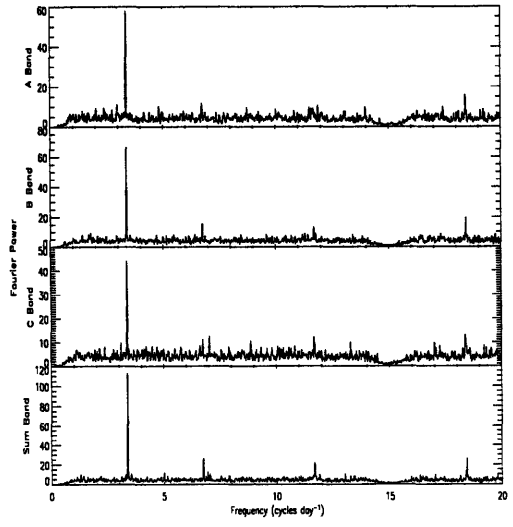

Figure 4-49: Power density spectrum of X1658-298

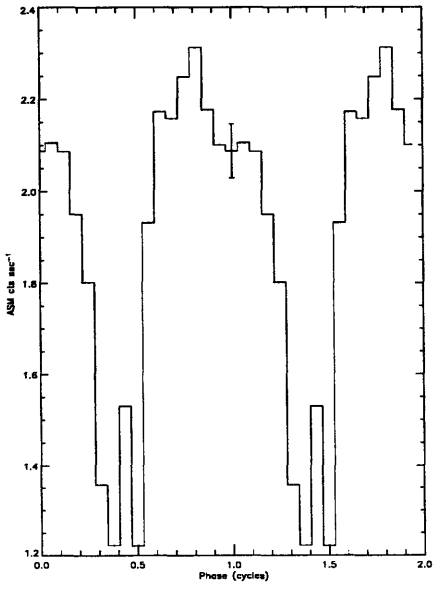

Figure 4-50: Folded lightcurve of X1658-298

and Corbet determined the period to be $P = 5.16329 \pm 0.00016$ hours. We have also detected this period in the sum band, and we determine it to be $P = 5.1634 \pm 0.006$ hours, consistent with the previous two detections.

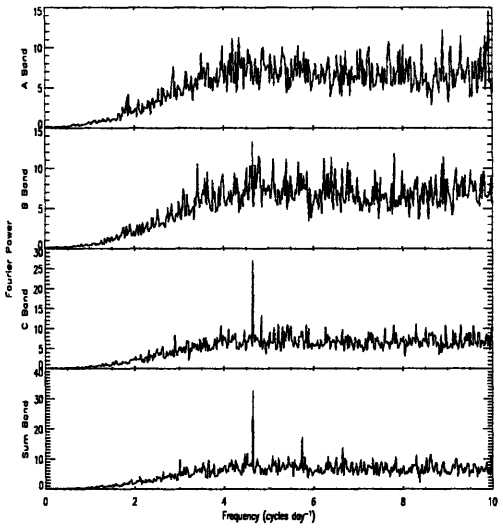

Figure 4-51: Power density spectrum of X1746-371

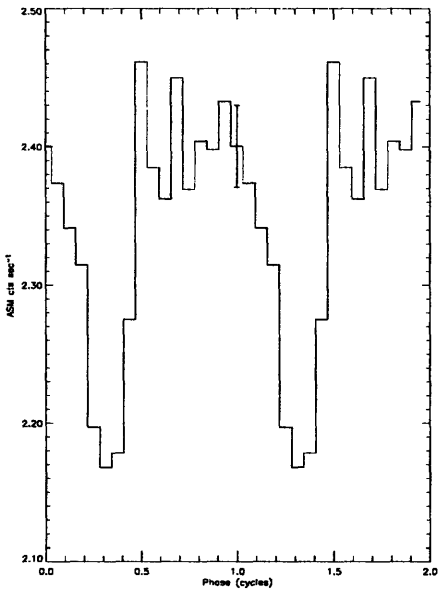

Figure 4-52: Folded lightcurve of X1746-371

X1820-303 is an LMXB bursting atoll source located in the globular cluster NGC 6624. It was discovered to exhibit a 176.4 ± 1.3 day period on the basis of *Vela 5B* data by Priedhorsky and Terrell (1984). Later, Stella *et al.* (1987) found a coherent 685 sec periodicity in *EXOSAT* data. This period was interpreted as the orbital period of the source rather than the 176.4 day period detected. Levine and Corbet (2006) detected this periodicity RXTE ASM data, and we also detect it in the sum band. We find the period to be $P = 11.41685 \pm 0.00001$ min.

X1822-371 is a LMXB containing a neutron star, the orbital period of which was first determined from optical observations by Seitzer *et al.* (1979). The source's X-ray period was discovered by White *et al.* (1981) on the basis of *HEAO 1* data to be $P = 0.232110 \pm 0.000003$ days. We detect the period in RXTE ASM data in all bands, and we find it to be at $P = 5.57421 \pm 0.00017$ hours.

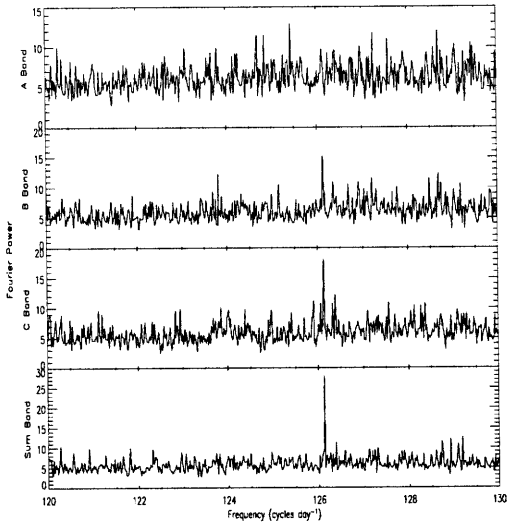

Figure 4-53: Power density spectrum of X1820-303

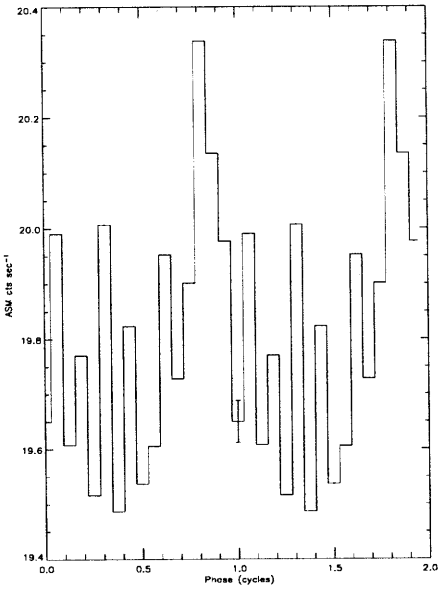

Figure 4-54: Folded lightcurve of X1820-303

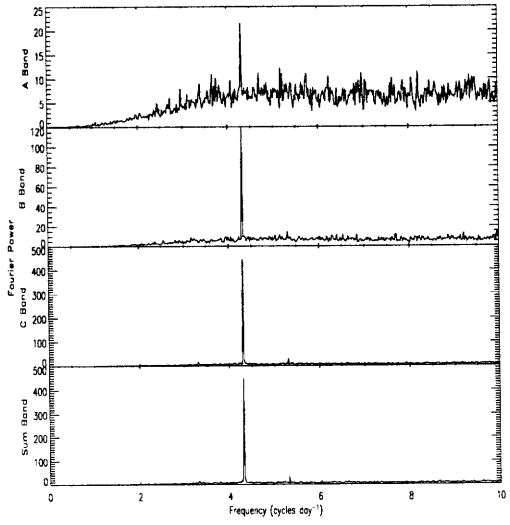

Figure 4-55: Power density spectrum of X1822-371

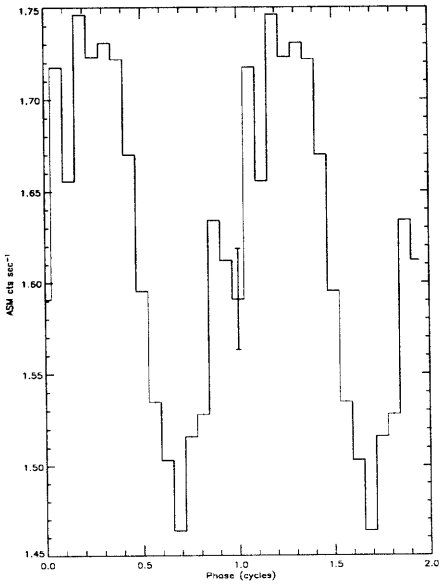

Figure 4-56: Folded lightcurve of X1822-371

X1916-053 is a bursting LMXB containing a neutron star. It is the most compact known dipping source. Its period was under dispute during the late 1980s, being confined to the range of $2985 - 3015$ sec (see, e.g., Wen *et al.* (2006) for details). The optical period of the source has been reported to be 3027.402 ± 0.42 sec by Grindlay *et al.* (1988). However, Callanan *et al.* (1995) report a stable 3000.6508 ± 0.0009 sec period in X-rays on the basis of ASM data. The most significant detection we report is consistent with being the first harmonic of the period reported by Callanan *et al.*. Our period derived from the strongest peak in the PDS of the sum band data, which was the first harmonic of the RXTE period, $P_{\rm harmonic} = 1500.3266 \pm 0.13$ sec. This period implies a fundamental of 3000.653 ± 0.007 sec.

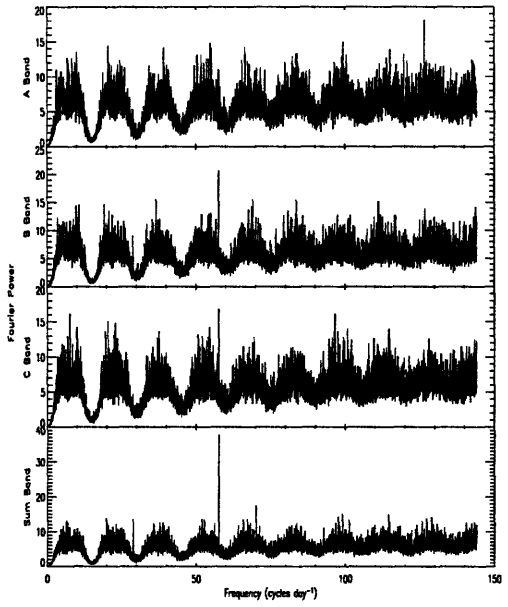

Figure 4-57: Power density spectrum of X1916-053

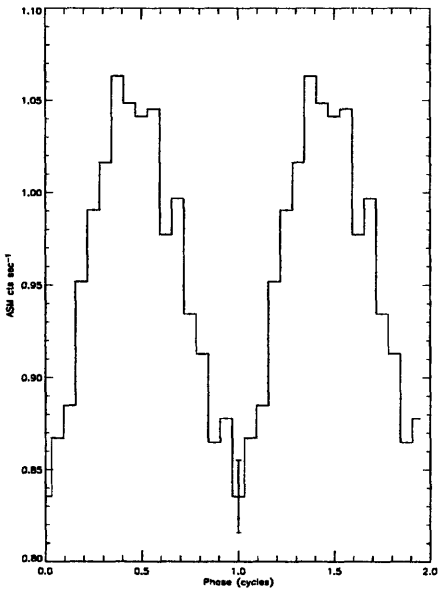

Figure 4-58: Folded lightcurve of X1916-053

X2127+119 is an accretion disk corona (ADC) dipping LMXB located in globular cluster NGC 7078. Anderson *et al.* (1989) report pulsations from the neutron star in the system with period $\sim$ 30 msec. Hertz (1987) reported an 8.66 ± 0.08 hour periodicity based on *HEAO 1* data, and this was attributed to the first harmonic of an earlier optical period. The X-ray period has been attributed to dipping induced

by the ADC at the orbital period. We have detected the period of the first harmonic of the orbital period to be at 8.5562 ± 0.0004 hours, implying an orbital period of $P = 17.1124 \pm 0.0008$ hours.

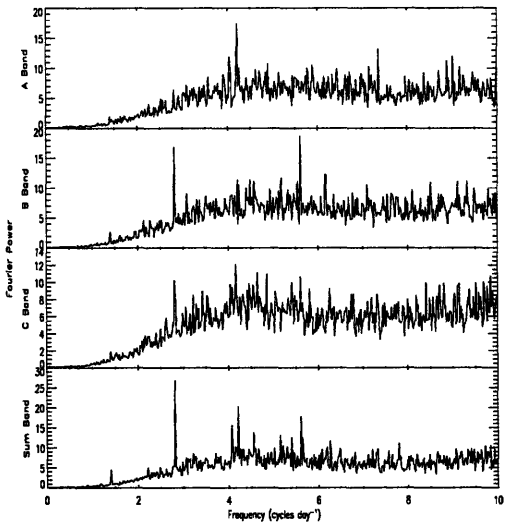

Figure 4-59: Power density spectrum of X2127+119

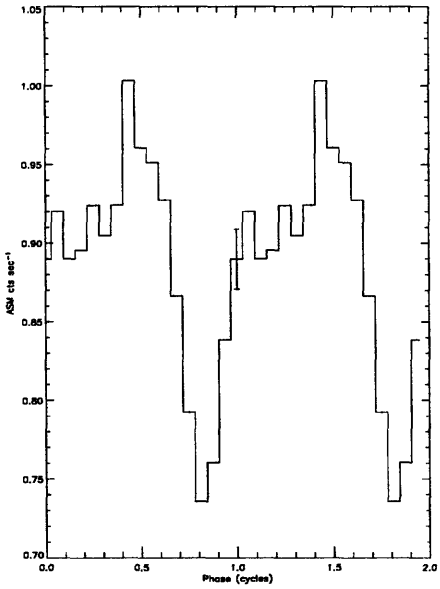

Figure 4-60: Folded lightcurve of X2127+119

4.3 Cataclysmic Variables

AM Herculis is an intermediate polar CV whose orbital period was discovered by Szkody and Brownlee (1977) to be 0.128927 ± 0.000002 days. Subsequent observations showed AM Her to contain a highly magnetic compact star, which was later identified to be a white dwarf, completing the identification of the object. We find a X-ray period of 0.128928 ± 0.0001 days in all bands.

4.4 Special Cases

IGR J21247+5058 is a type 1 Seyfert galaxy only recently discovered to be an AGN. Molina *et al.* (2006) have analyzed the spectrum of the source, which they describe

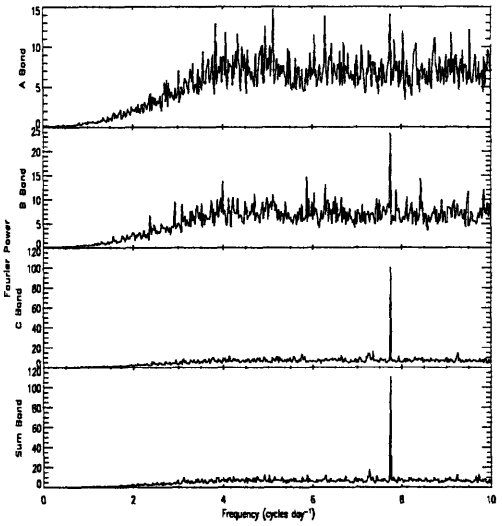

Figure 4-61: Power density spectrum of AM Her

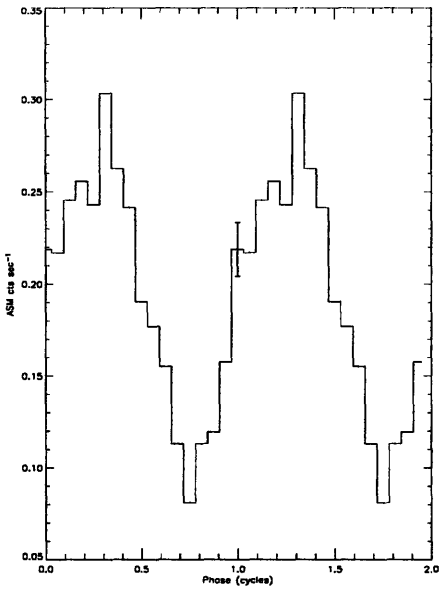

Figure 4-62: Folded lightcurve of AM Her

as "puzzling." They ascribe the source's spectrum to an alignment of a radio galaxy at a redshift of $z \approx 0.02$ and a foreground, relatively nearby, star. We detect an X-ray periodicity in the C band with $P = 3.23097 \pm 0.0022$ hours. This detection is consistent with a foreground LMXB against a radio galaxy background, although the liklihood of such a conjunction of a LMXB and radio galaxy seems small. This detection is significant at a 92% level.

Having presented the results of the general periodicity search, we move on to give motivation for a general time-variable modulation search by presenting findings from the summer of 2006. We have found that the Galactic bulge atoll source GX 9+9 exhibits significant changes in modulation strength over time. This fact presents a puzzle and motivates a search for other sources with such behavior.

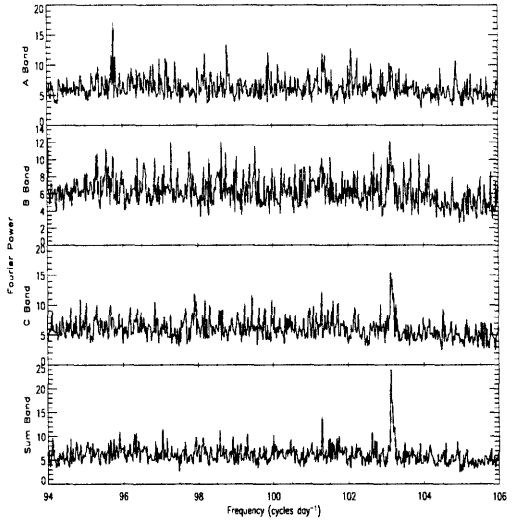

Figure 4-63: Power density spectrum of X Per

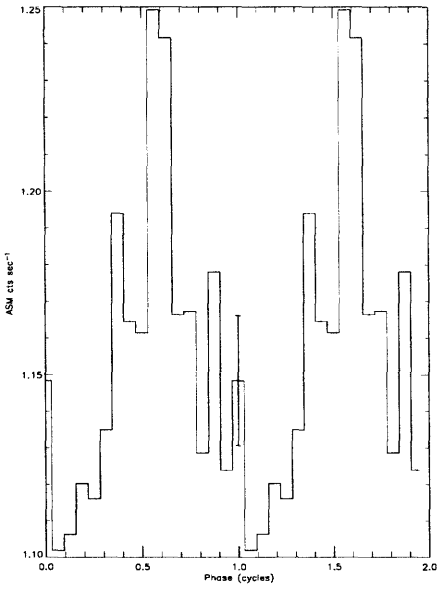

Figure 4-64: Folded lightcurve of X Per

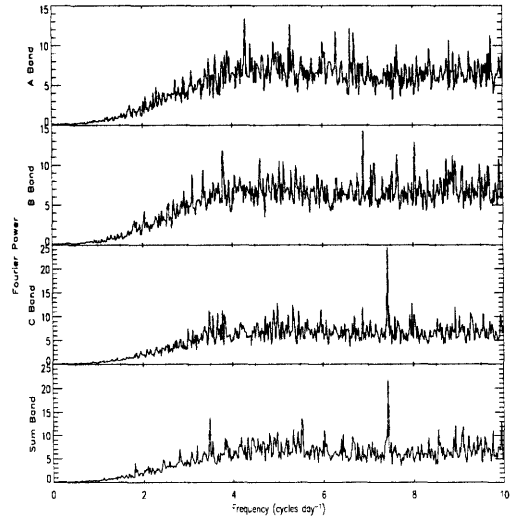

Figure 4-65: Power density spectrum of IGR J21247+5058

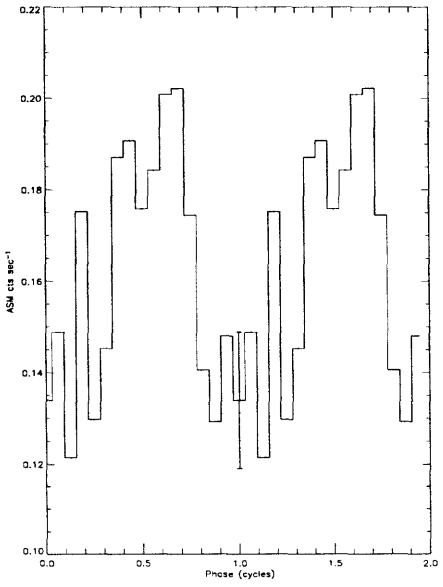

Figure 4-66: Folded lightcurve of IGR J21247+5058

Chapter 5

Unusual Time-varying Modulation Strength in GX 9+9

In this chapter, we present a detailed picture of the Galactic bulge atoll LMXB GX 9+9. The level of detail we provide is warranted by the peculiar nature of the X-ray modulation at the orbital period in this source, specifically its time-varying strength. In dipping sources, such as X1254-690, such behavior is common; however, there has been no evidence to support the conjecture that GX 9+9 is a dipping source.

We begin by summarizing dynamical information about the system and results from previous observations of the source. We then proceed to present ASM observations demonstrating peculiar behavior in GX 9+9 along with pointed PCA observations showing the same. Finally, we present a *Chandra* lightcurve of the source from an observation in 2002 and a short discussion of other sources that exhibit similar behavior, but in the optical.

5.1 Information on GX 9+9 and Results of Previous Observations

The LMXB GX 9+9 is a Galactic bulge atoll source located at $b^{II} = 8.51°, l^{II} = +9.04°$ and estimated to be approximately 7 kpc away from the Sun. A periodicity

of 4.19 ± 0.02 hours in the X-ray flux from GX 9+9 was discovered in *HEAO A-1* data by Hertz and Wood (1988). They found that the modulation at this period was approximately 4% of the average source intensity and that the modulation was significant at the 99% level. They interpreted the modulation as indicative of the orbital period of the binary system. Under the assumption that the system consists of a Roche lobe filling companion in an orbit around a 1.44 $M_{\odot}$ neutron star, they derived that the primary was an early M dwarf with mass $0.2 - 0.45$ $M_{\odot}$ and radius $0.3 - 0.6$ $R_{\odot}$. They were also able to set an upper bound and an estimate on a lower bound on the orbital inclination of $50° \leq i \leq 63°$.

Optical results obtained by Schaefer (1990b) showed that the counterpart of GX 9+9 had an orbital period of 4.198 ± 0.0094 hours with approximately equal modulation amplitudes in the B, V, and R bands. Schaeffer used this data to confirm the binary parameters derived by Hertz and Wood, with the notable addition that the orbital separation was determined to be $a = 1.6 R_{\odot}$.

In a recent paper, Kong *et al.* (2006) reported results from a nearly simultaneous observing run of GX 9+9 in both the optical and the X-ray bands. Their results showed that while clear optical modulation was present as of 1999, X-ray modulation was not found in the RXTE PCA data in either the $2 - 3.5$ keV or the $9.7 - 16$ keV range during that time. In addition to their pointed PCA observation, Kong *et al.* also reviewed archival data from a 14.4 hour observation of GX 9+9 made with *EXOSAT* in 1983, a 6.6 hour observation made with *ASCA* in 1994, and a 6.4 hour observation made with *BeppoSAX* in 2000. They found no significant detection of the 4.19 hour periodicity in any of the above X-ray observations.

In the next section, we present X-ray data from the ASM indicating that the 4.19 hour modulation of GX 9+9 is currently "on" and that it only turned on around March of 2004.

5.2 ASM Results

The ASM light-curve of GX 9+9, as shown in Fig. 5-1, shows a relatively strong source that has brightened since the beginning of the RXTE mission, but which also has undergone some modulation in its intensity over long timescales. This behavior is similar in all three subbands. The detection of the orbital periodicity in ASM data was first reported by Shivamoggi (2005). Acting on a request by Dr. Osmi Vilhu of the University of Helsinki, we analyzed the light-curve of GX 9+9 to determine if time-variable modulation was exhibited by the source, using the procedure of smoothed-subtraction as outlined in Chapter 3.

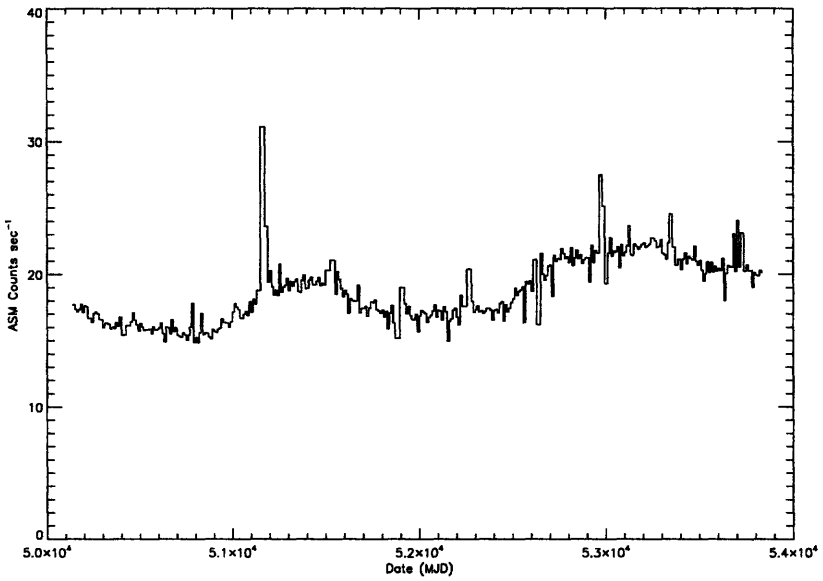

Figure 5-1: ASM sum band light curve of GX 9+9.

We took the data from the ASM (approximately 10 years worth of data as of March, 2006), and we divided it into 10 equal time intervals with the first such interval starting at MJD 50100 and the last such interval ending at MJD 54000. After performing the smoothed-subtraction technique, we calculated power density spectra for each of the 10 resultant light curves. It was found that only in 3 of the 10

~1.1 year intervals was the periodicity significantly detected. We present the power density spectrum of each of five equally long segments of ASM data on GX 9+9 from the sum band in Fig. 5-2, where the first segment is at the top and the last at the bottom. It is plainly clear that the modulation strengthened considerably during the

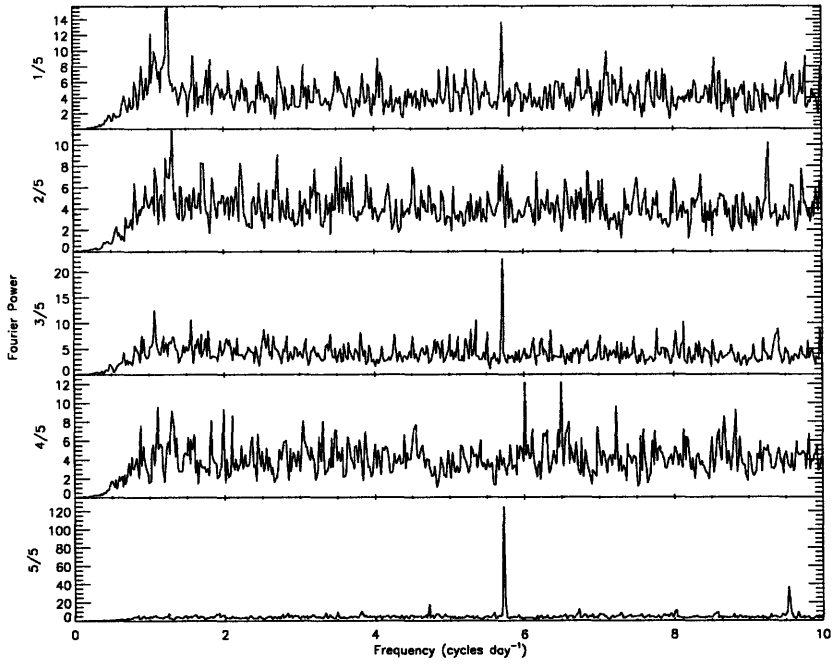

Figure 5-2: Power density spectra of ~ 2 year segments of ASM observations of GX 9+9.

fifth time segment. Given that the orbital period was previously known, we classify the peak in the third time segment as a detection, though it is significantly weaker than the detection in the last time segment. Folded light curves demonstrating this behavior on shorter timescales are shown in Fig. 5-3, where we have divided the entire ASM lightcurve of GX 9+9 into 30 pieces, each comprising approximately 133 days worth of data. We then folded each ~ 133 day interval separately on the orbital period of 4.19344 hours, a refinement of the 4.19 hour period as determined by Levine and Corbet (2006). In the figure, all vertical axes have the same scale and offset, as do all horizontal axes. The numbers in the top left corner indicate from which interval the data comes, with "1" indicating data from the first ~4 months, etc. Typical

errors for each lightcurve are shown near phase 1.0. Note the sudden appearance and disappearance of the periodic modulation in panel 16.

5.2.1 Energy Independence of the Modulation

One peculiar aspect of the modulation in GX 9+9 is the fact that the modulation is energy independent. This is expected for eclipsing events, where all photons from the central source are blocked. However, eclipsing events are not consistent with the transient nature of the modulation. This transient nature is consistent with some dipping sources. However, because most dipping is energy dependent, as would be expected if it were caused by an increase in column density along the line of sight to the source, the energy independence of the modulation strength is not consistent with GX 9+9 being a dipping source.

In Fig. 5-4, we present a measure of color as a function of orbital phase where we have taken the folded lightcurve for data from the last year of ASM observations used in our analysis and performed binwise division for the three possible colors using ASM data. One can see that the resultant hardness ratios are consistent with no change in color.

In addition to the data from the ASM, we were also able to analyze data from the PCA. These data confirm the results obtained from the ASM, namely that flux modulation at the orbital period of GX 9+9 was not significant before March of 2004 but was significant as of the middle of 2006.

5.3 PCA Results

Subsequent to our discovery of the strengthening of the X-ray flux modulation in June 2006, a PCA observation of GX 9+9 that lasted for approximately 10 hours was conducted on June 20, 2006. Shown in Fig. 5-5 are the results of the observation in three different energy bands. One can see that the PCA data show the strength of the modulation to be energy-independent to a good approximation and the phase of the minima to be stable, thus corroborating the results from the ASM data.

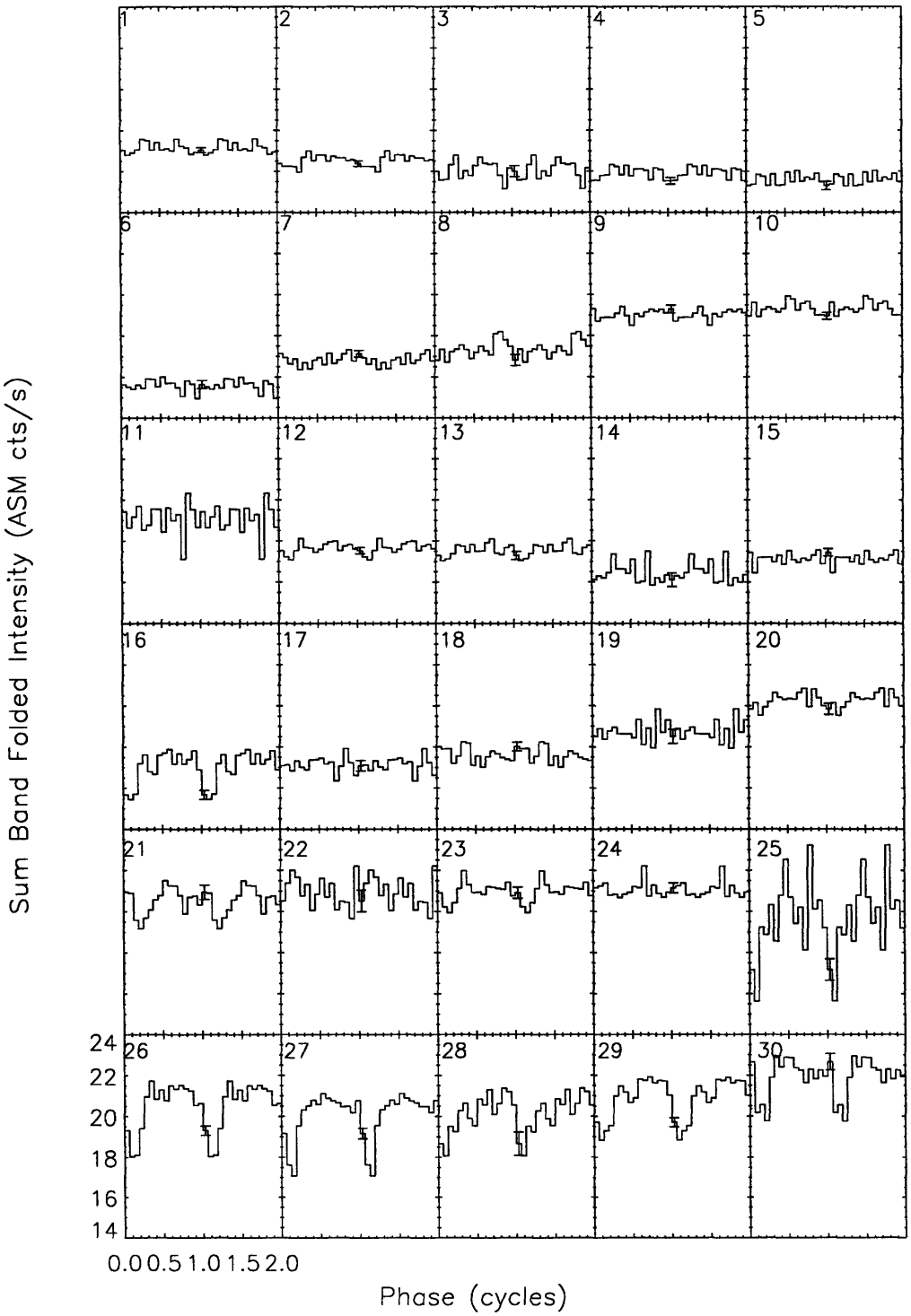

Figure 5-3: Folded light curves from ASM 2-12 keV observations of GX 9+9.

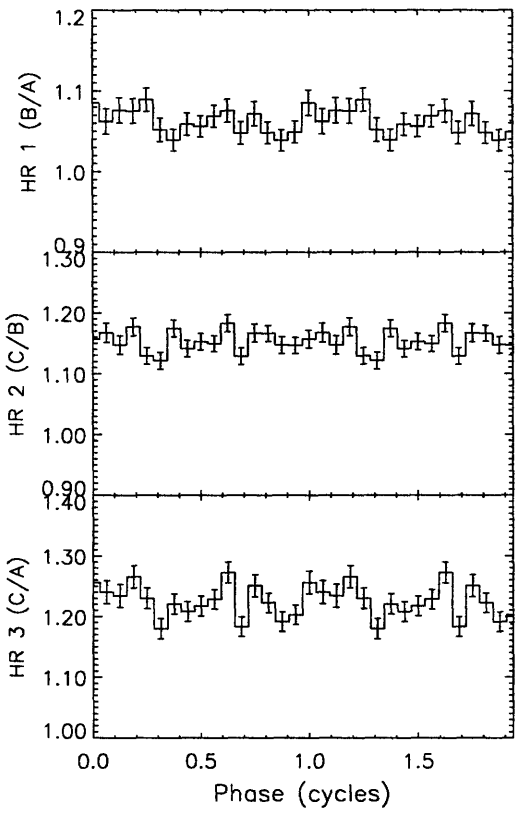

Figure 5-4: Hardness ratios implied by bin-wise ratios of folded intensities during last year of ASM data.

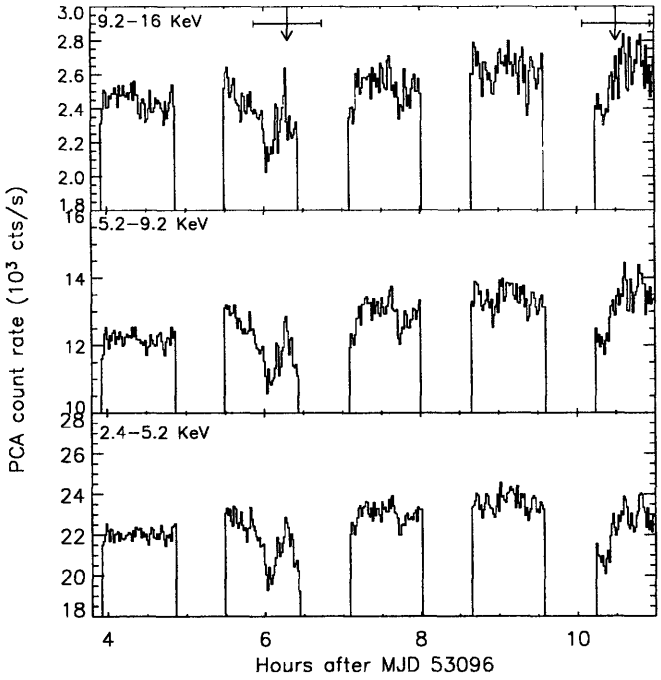

Figure 5-5: PCA Observation of GX 9+9 taken on June 20, 2006 (ID 92509-01-01-00).

After this observation, we looked back at archival PCA data on GX 9+9 to see if any of the previous observations contained evidence of the orbital modulation. We restricted our analysis to observations of length at least 0.25 orbital cycles (about 1 hour) so we had a reasonable chance of finding a time during which there was both source coverage (i.e. not during an Earth occultation) and during which we predicted a minimum in the X-ray light curve. There were 29 such observations comprising $\sim$ 460 ksec, with approximately half of the observations taking place in the time period 1996-1999 and the rest taking place in the time period 2002-2004. There is no evidence of the periodicity in any of the ASM data from these times, so we expected not to find any evidence for it in the PCA data either.

We folded the data from the 29 observations at each of a grid of closely spaced periods centered on our best estimate of the orbital period from the ASM data. We did this for the energy bands 2-5, 5-12, and 12-30 keV. We computed a χ^2 statistic for each folded lightcurve and plotted the results against folding period. No significant peaks were found. Thus we found no evidence of the 4.19 hour periodicity in the PCA data.

However, while the folding analysis did not yield any evidence for persistent modulation that was stable in phase, upon examination of the individual observations, we found cases where dips did occur that were consistent with the phase of the modulation as seen in ASM data. We also saw many cases in which there was no modulation at all during the observation and cases where dips occurred at a phase not consistent with the phase we see for modulation in the ASM light curves. Some of these PCA observations are shown in Fig. 5-6 and Fig. 5-7.

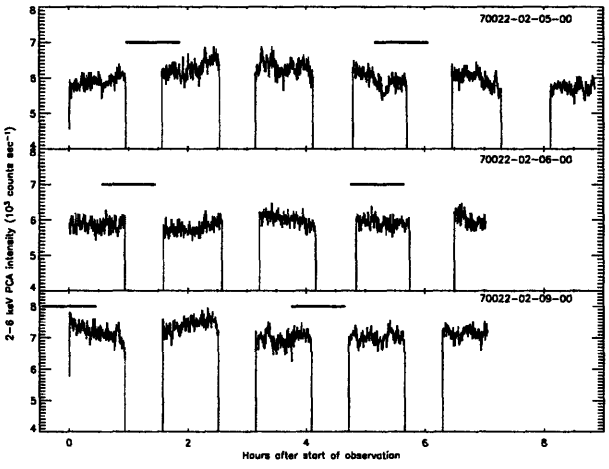

Figure 5-6: 3 PCA observations of GX 9+9. From top, they begin at 09:00:00 UT on 6 June, 2002, at 11:00:00 UT on 11 June, 2002, and at 18:00:00 UT on 29 April, 2004. The observation IDs are located in the top right corners of the plots. The bars above the lightcurves indicate the centers and uncertainties of location of the expected dips. The April 2004 observation was done shortly ($\sim$3 months) before modulation started to increase dramatically in GX 9+9. Note the slight dip in the observation of June 6, and that no dip is observed during the other observations.

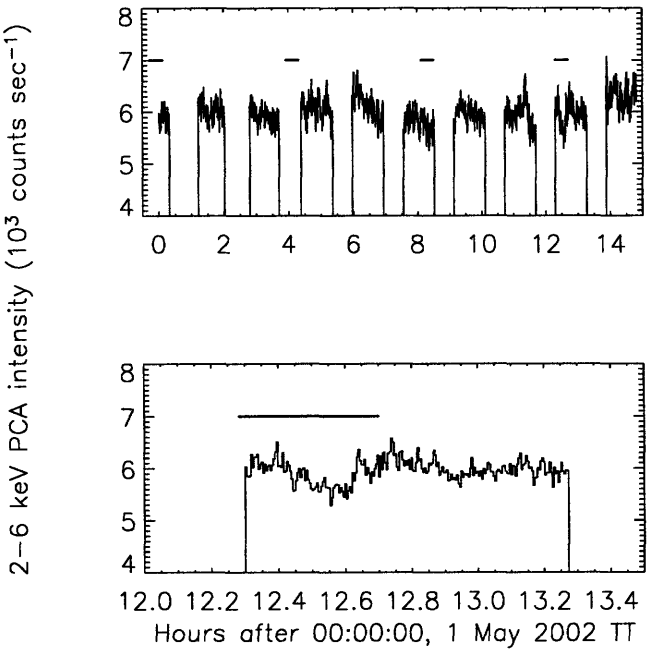

Figure 5-7: PCA observation of GX 9+9 starting at 14:00:00 on 1 May 2002. Note that there is one possible dip in the upper plot at $\sim$ 8.25 hours which is consistent with the phase of the ASM dip and there is another, more noticable dip at 12.5 hours. The second dip is shown below, blown up for detail. For reference, ASM data from May 2002 are folded in panel 18 of figure 1.

The data from the PCA observation of June 20, 2006, allow us to see whether the modulation from GX 9+9 is, in fact, stable in phase despite not being so in amplitude. The phase location of the minima of the ASM light curves is approximately 0.1 cycles with a reference epoch of MJD 50100 and a period of 4.19344 ± 0.00002 hrs. Thus, the start of the PCA observation was 3806.3 days after the reference time for the ASM fold. This implies that 21784.3107 cycles of the source passed from the reference date to the start of the PCA observation. Thus, phase zero occurs again at MJD 53906.246 ± 0.436 hours. Phase zero then occurs at 5.90 hours and 10.09 hours during the observation. This imples that minimum X-ray flux should occur at 6.31 hours and 10.51 hours, with an uncertainty in both of 0.436 hours. These times are shown in Fig. 5-5 with error bars, and, indeed, dips in the intensity in all three energy bands can be seen within the errors of the estimates.

5.4 *Chandra* Observations of GX 9+9

We have also reviewed archival *Chandra* observations of GX 9+9. There was one such observation starting on 22 August, 2000, at 05:20:21 UT (MJD 51778.2225) carried out with the ACIS instrument. During the $\sim$ 20 ksec observation (see Fig. 5-8), there appeared to be slight modulation; there were two slight minima in the X-ray light curve with approximate amplitude 4 %, similar to that found by Hertz & Wood (1987). They were also approximately 15 ksec apart, so it was possible that the *Chandra* observation indicated dips where the PCA and ASM did not. However, in all the data we have, the orbital modulation of GX 9+9 has appeared to remain approximately stationary in phase during all times at which it is visible. From an analysis of the ASM data with a date of minimum X-ray flux of MJD 53455.1187 as determined from panel 26 of Fig. 5-3, we have determined that the minimum should occur at 11.32 ± 2.5 ksec in the observation. The minima predicted from the ASM data are approximately 5 ksec (0.33 orbital cycles) away from where the minima we observe in the *Chandra* observation lie. This discrepancy seems to indicate that what we observe in the observation is not the orbital modulation. This fact follows because

the PCA lightcurve seems to indicate that the orbital modulation is stable in phase. Also, the PCA and ASM indicate that the source's modulation was not detectable during the *Chandra* observation. In addition, the depth of the minima in the *Chandra* lightcurve is within the limits of photon counting statistics. Hence, we have found no evidence of orbital modulation of GX 9+9 in the *Chandra* observation.

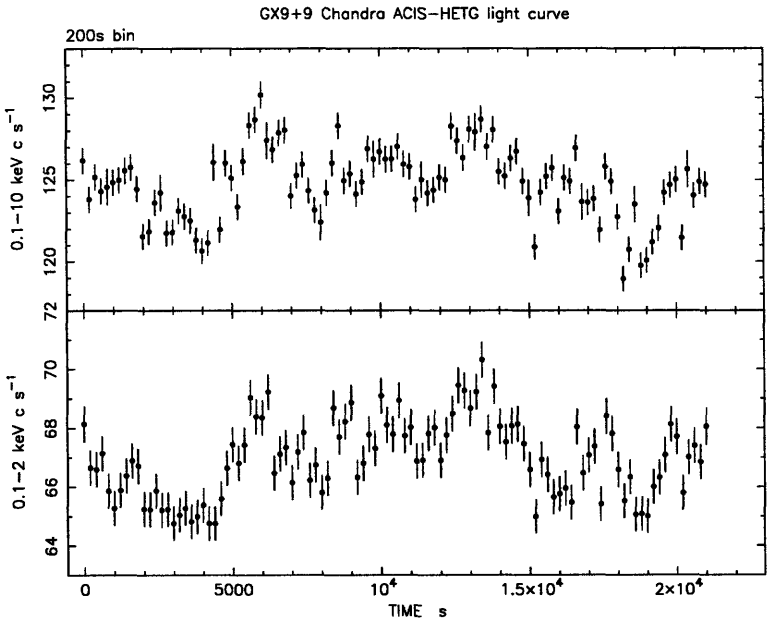

Figure 5-8: *Chandra* observation of GX 9+9.

5.5 Interpretation of variable modulation

We have recently found changes in the amplitude of the orbital modulation in the bright Galactic bulge atoll-type LMXB GX9+9. Similar behavior has been observed in dipping sources such as X1746-370 and X1254-690. However, apart from these cases, there are not many studies in the literature of changes in the degree of modulation at the orbital period. GX9+9 has not been reported to exhibit dips, and the causes of its orbital modulation are not determined.

Similar behavior, however, has been exhibited in the optical. In particular, the LMXBs X1957+115, MS 1603+26, and X1916-053 all have shown markedly different light curves with respect to both structure and amplitude during different epochs. Whether similar mechanisms might produce the behavior in the optical and in the X-ray is unknown. Such behavior could arise from accretion disk instabilities in the source, but it is difficult to say for certain, and more work needs to be done to determine the cause of GX 9+9's variable modulation strength.

THIS PAGE INTENTIONALLY LEFT BLANK

Chapter 6

Results of Time-Variable Modulation Search in RXTE ASM Data

In this chapter, we present the results of a search for time-variable modulation in X-ray sources using RXTE ASM data by employing the smoothing-subtraction method. We have divided the sources' lightcurves into three pieces each and used the following criterion. If a periodicity in some energy band is significant in the power density spectrum of the data belonging to one time period and it is not in another, we consider it a candidate for a source undergoing time-varying modulation strength. We then appeal to the folded lightcurves of the source for each segment of the ASM data to decide whether it indeed exhibits such behavior.

Below, we present the findings by type of object, give a limited discussion of the details of the systems if not already described in the previous chapter, comment on the significance of the modulation, and give the relevant periods found in the periodicity search.

6.1 High Mass X-ray Binaries

Centaurus X-3 is a HMXB that was described in Chap. 4. We have found that the modulation strength decreases monotonically with time. It seems most likely that this is not due to an intrinsic variation in the source, but rather to the fact that the ASM is becoming less sensitive as it spends more time in space. The modulation is detected at $P = 1.0434 \pm 0.0002$ days, the first harmonic of the orbital period.

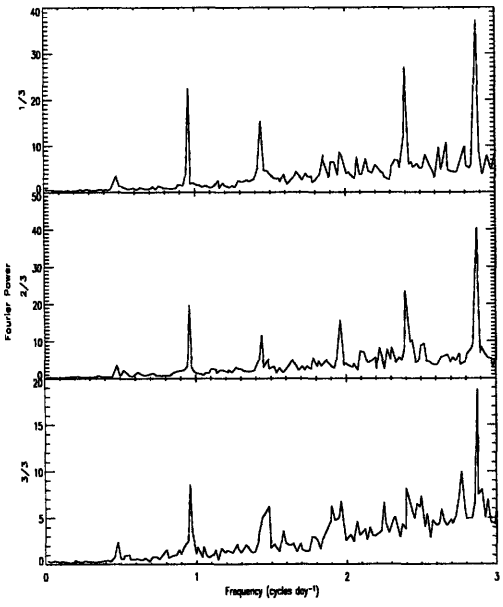

Figure 6-1: Power density spectra of Cen X-3

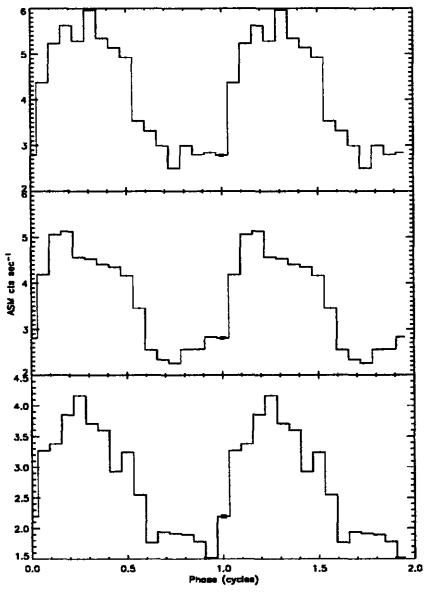

Figure 6-2: Folded lightcurves of Cen X-3

Hercules X-1 was described in Chap. 4. The source appears to have undergone a reduction in the source modulation strength since the beginning of the mission.

RX J0146.9+6121 is a Be/HMXB system with a neutron star that was at one time the pulsar with the slowest rotation period known. A $\sim$ 25 min periodicity was detected by White *et al.* (1987) using data from *EXOSAT*, but White *et al.* attributed the modulation to a nearby source, X0142+614. Mereghetti *et al.* (1993) detected the 25 min modulation in the *ROSAT* All-Sky Survey and attributed it to RX J0146.9+6121. This pulsar was detected to have spun-down by 1998 to a spin period of 1407 sec or 23.46 min (Haberl *et al.*, 1998). We have detected what might

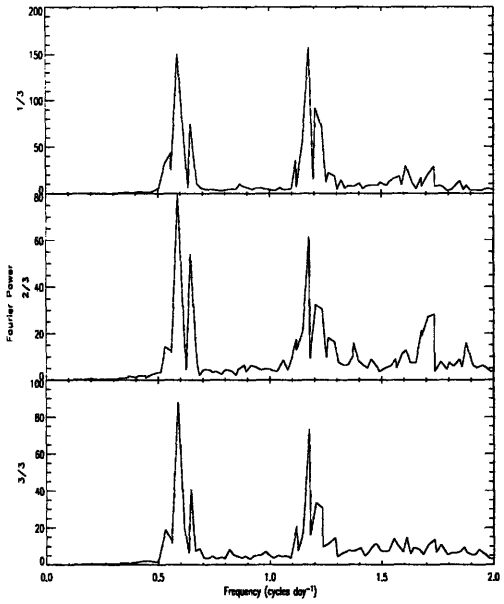

Figure 6-3: Power density spectra of Hercules X-1

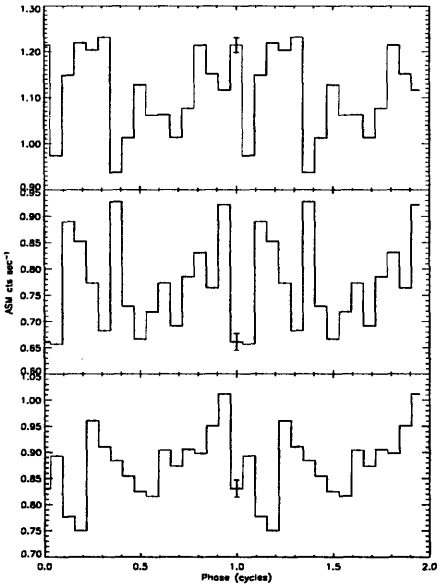

Figure 6-4: Folded lightcurves of Hercules X-1

be the first harmonic of the pulse period in the final third of all RXTE ASM data, $P = 12.42960 \pm 0.00003$ min. This implies a fundamental of 24.85920 ± 0.00006 min. We believe this is probably a real detection of the pulse period, although the power does not meet the formal criterion for significance, due to fact that the pulsar has a history of spinning-down.

X0114+650 is a SG/HMXB, and the system was described in detail in Chap. 4. During the first third of ASM data, we detect the pulsation period at 2.7402 ± 0.0008 hours. However, during the second third, evidence for such modulation disappears. Interestingly, a modulation reappears in the third segment of ASM data, but at a different period, $P = 3.8496 \pm 0.0006$ hours. Corbet *et al.* (1999) analyzed RXTE ASM data and found the pulse period of the source slightly slower than the 2.78 ± 0.01 hours previously reported. They also found multiple peaks in the PDS near to their detected pulse period, and this finding led them to investigate whether the frequency shifted in time. They found slight frequency shifts (on the order of a few tenths of a percent) when they divided all ASM data to that point into five equally long pieces

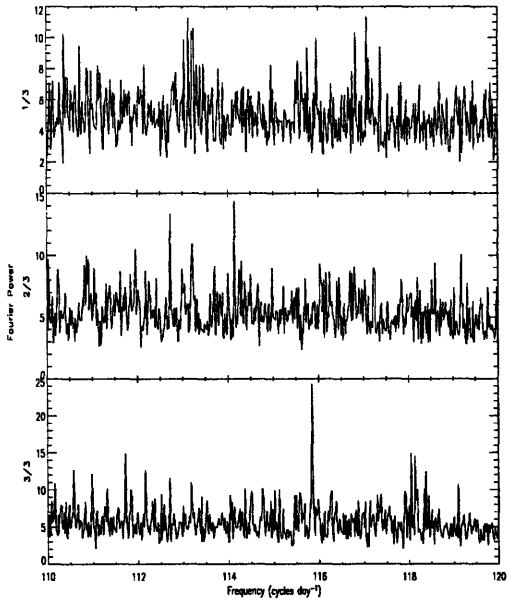

Figure 6-5: Power density spectra of RX J0146.9+6121

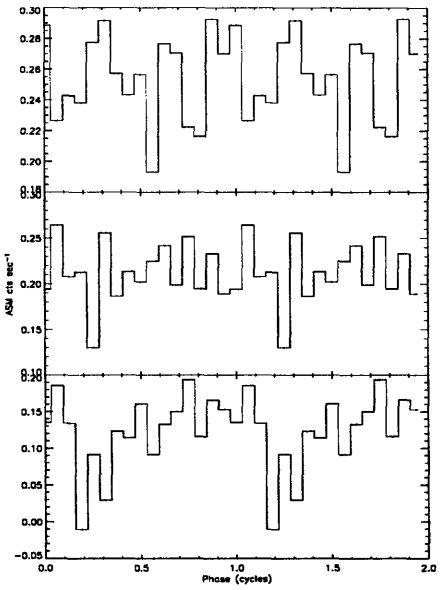

Figure 6-6: Folded lightcurves of RX J0146.9+6121

and Fourier analyzed each. If the period detected in the third segment of ASM data is indeed a new pulsation period for the neutron star in the system, this implies that a major spin-down event occurred during the intervening years in the system.

X1953+319 is a LMXB comprising a neutron star and a suspected M-type giant — one of only three LMXBs known or suspected to contain such a companion. Corbet *et al.* (2006) report a detection of a $\sim$ 5.09 hour periodicity in *Swift* Burst Alert Telescope data. After further analysis, they found that, over the course of the mission, the signal in the PDS associated with the periodicity moved from 5.19 hours to 5.02 hours almost monotonically. We detect the period at about $P = 5.22 \pm 0.01$ hours in the second segment of the ASM data. The broad peak in the PDS probably indicates the time-variable nature of the frequency.

6.2 Low Mass X-ray Binaries

EXO 0748-676 is a LMXB that was described in Chap. 4. Modulation at the previously detected orbital period can be seen to have strengthened since the beginning

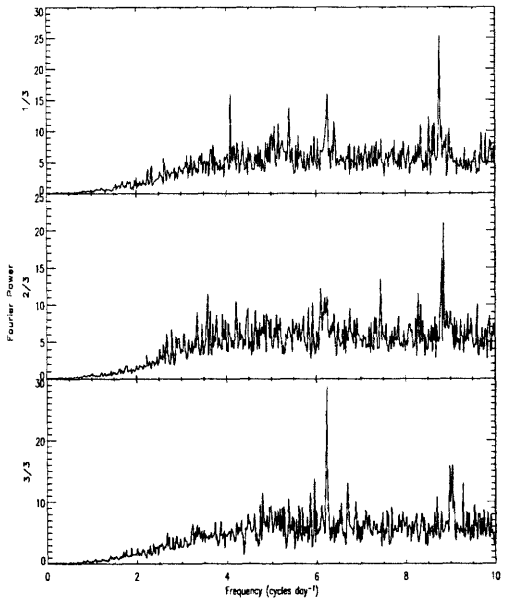

Figure 6-7: Power density spectra of X0114+650

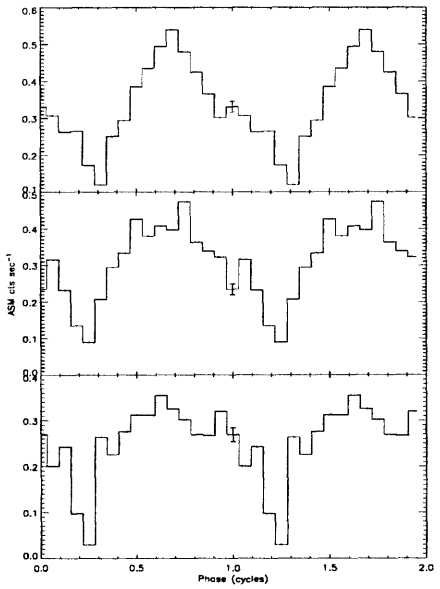

Figure 6-8: Folded lightcurves of X0114+650 ($P = 2.78$ hours)

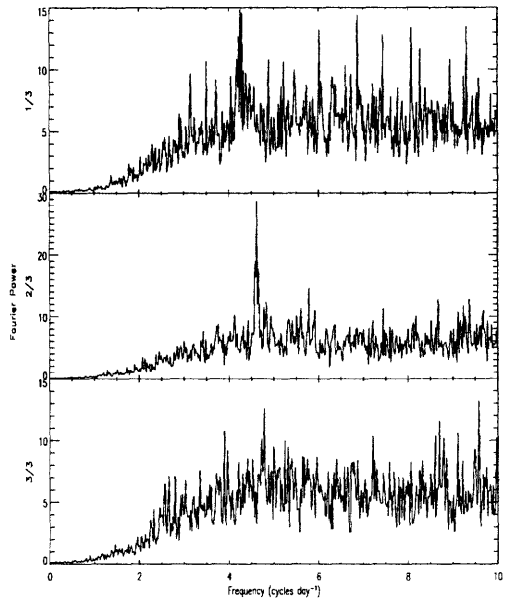

Figure 6-9: Power density spectra of X1953+319

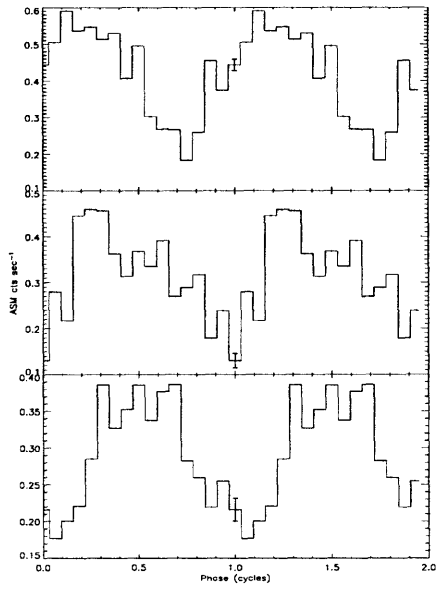

Figure 6-10: Folded lightcurves of X1953+319

of the third segment of the ASM data.

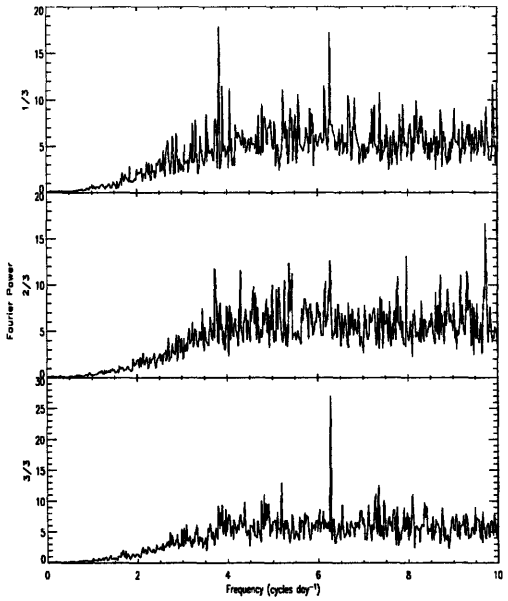

Figure 6-11: Power density spectra of EXO 0748-676

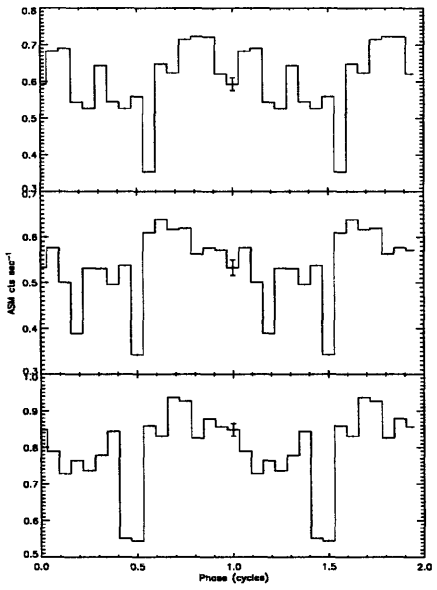

Figure 6-12: Folded lightcurves of EXO 0748-676

GX 9+9 is an atoll LMXB that was thoroughly described both in Chap. 4 and Chap. 5. Therefore, we will only present a plot of the PDS.

X1636-536 is an neutron star LMXB which is a bursting atoll source. Its orbital period was determined from optical modulations by Pedersen *et al.* (1981) to be ~ 3.8 hours. Levine and Corbet (2006) determined the X-ray period to be 3.79315 ± 0.00006 hours on the basis of RXTE ASM data. We confirm this result, but we find that the source is only detectable during the first third of the mission. We find the period to be $P = 3.7765 \pm 0.0001$ hours.

X1658-298 is a transient X-ray source that was quiescent from the beginning of the RXTE mission until 1999. This source was described in detail in Chap. 4. Since data on this source for the first third of the mission were unavailable due to the source's quiescence during this time, we have divided the data into two segments for the analysis. The periodic signal appears only in the last third of the mission in the sum band at $P = 7.116 \pm 0.001$ hours.

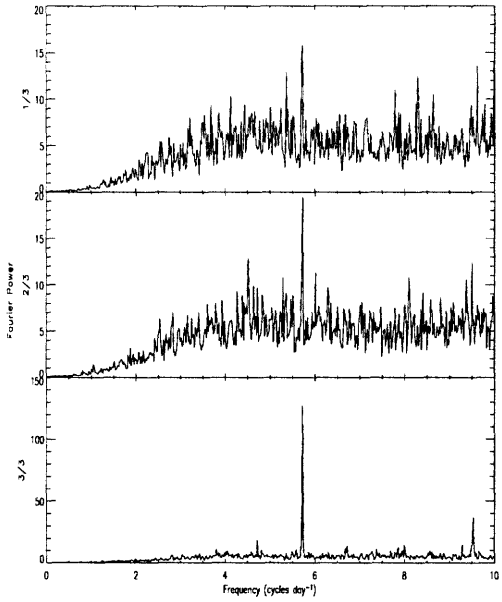

Figure 6-13: Power density spectra of GX 9+9

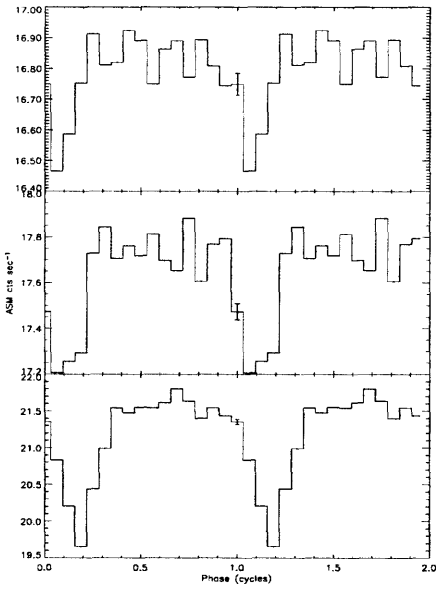

Figure 6-14: Folded lightcurves of GX 9+9

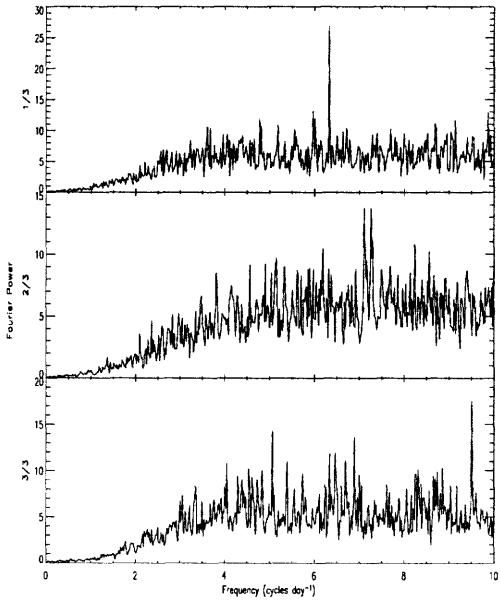

Figure 6-15: Power density spectra of X1636-536

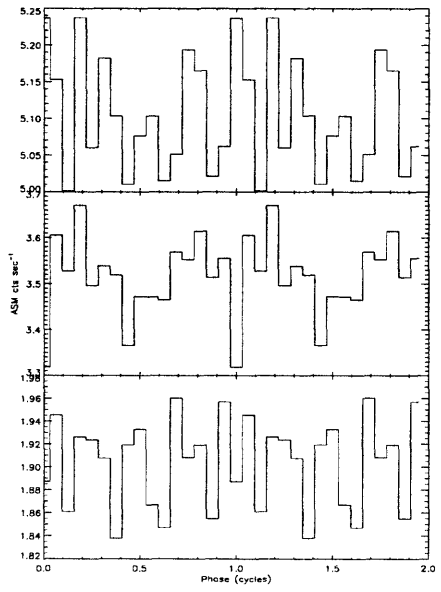

Figure 6-16: Folded lightcurves of X1636-536

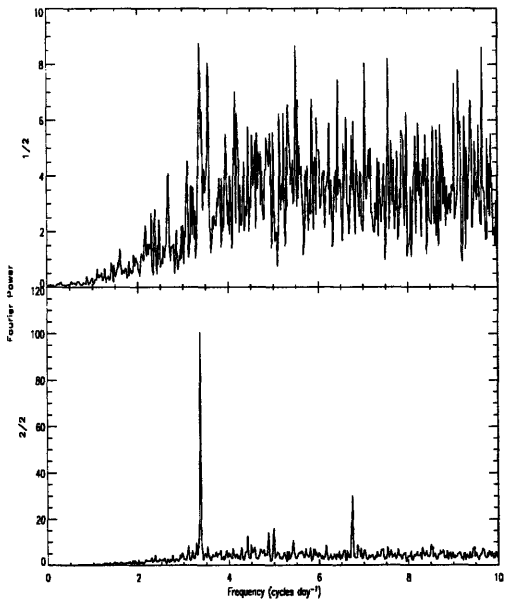

Figure 6-17: Power density spectra of X1658-298

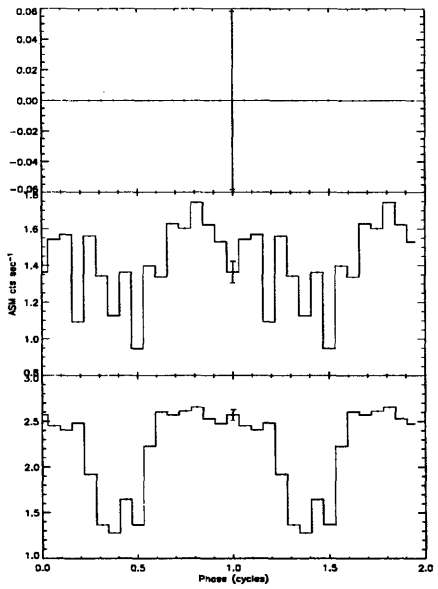

Figure 6-18: Folded lightcurves of X1658-298

X1916-053 is a neutron star containing LMXB which was described in Chap. 4. We find that the signal at the orbital period as well as at that of its subharmonic seems to have become less significant from the beginning of the mission until it is almost undetectable in the third segment of data. We find a period of 3000.653 ± 0.009 sec.

X2127+119 is a neutron star containing LMXB which was described in Chap. 4. We find that the orbital modulation is variable in its Fourier amplitude, with it starting strong in the first part of the mission and declining throughout the mission. The orbital period is detected at $P = 16.845 \pm 0.004$ hours.

6.3 Cataclysmic Variables

AM Herculis, as mentioned in Chapter 4, is a polar CV. We have found that the modulation mentioned in Chapter 4 only is detectable in ASM data during the first two thirds of the mission. During the last third, the X-ray modulation is undetectable in any energy band. When the period is detected, it is detected at $P = 3.0943 \pm 0.0002$ hours

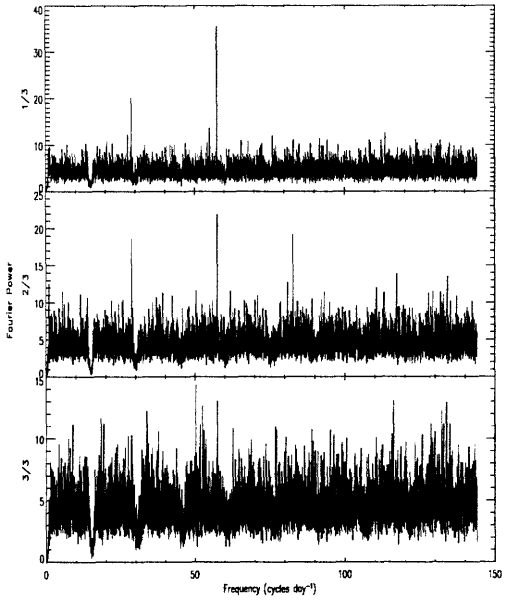

Figure 6-19: Power density spectra of X1916-053

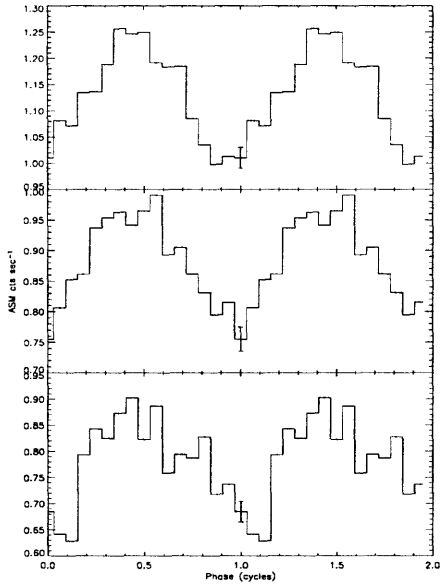

Figure 6-20: Folded lightcurves of X1916-053

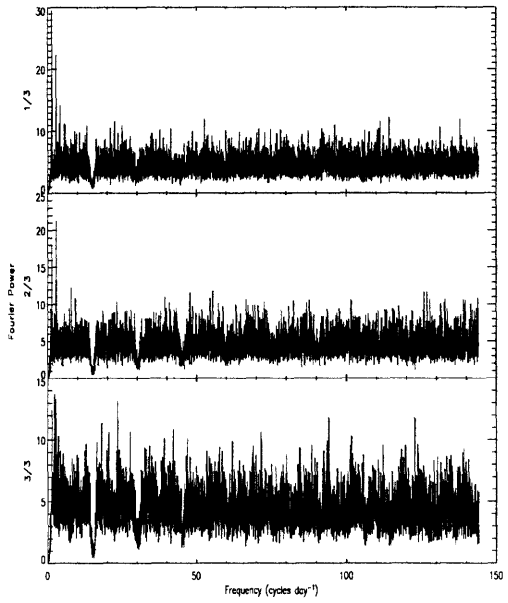

Figure 6-21: Power density spectra of X2127+119

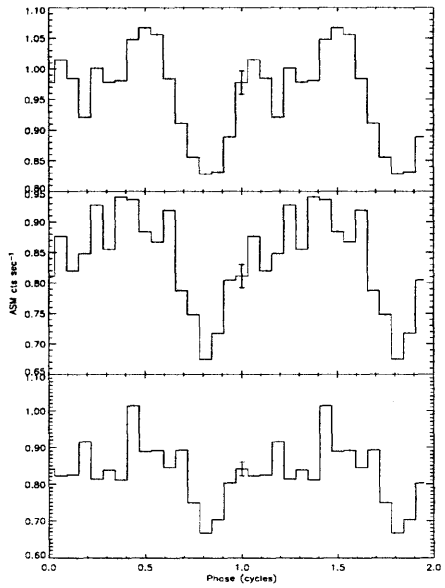

Figure 6-22: Folded lightcurves of X2127+119

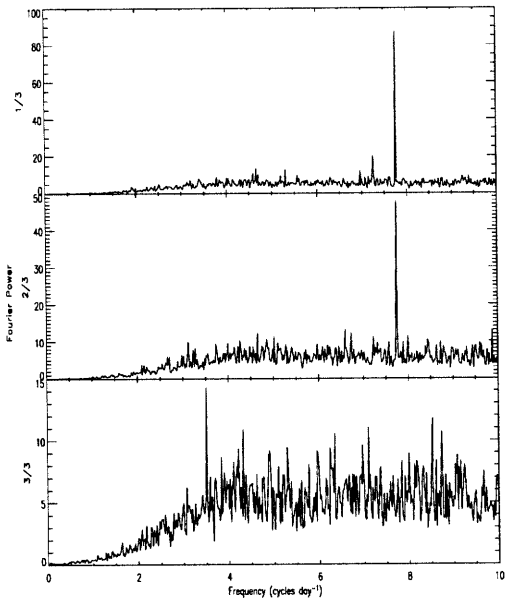

Figure 6-23: Power density spectra of AM Her

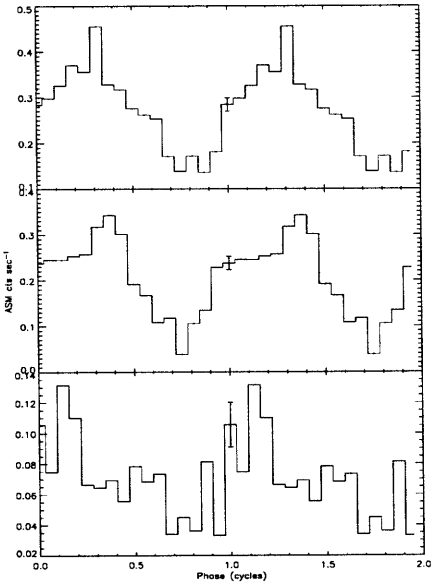

Figure 6-24: Folded lightcurves of AM Her

Bibliography

Anderson, S., Gorham, P., Kulkarni, S., Prince, T., and Wolszczan, A. (1989). PSR 2127+11C. IAU Circ., **4772**, 1–+.

Bailyn, C. D., Orosz, J. A., Girard, T. M., Jogee, S., della Valle, M., Begam, M. C., Fruchter, A. S., Gonzalez, R., Ianna, P. A., Layden, A. C., Martins, D. H., and Smith, M. (1995). The Optical Counterpart of the Superluminal Source GRO:J1655-40. Nature, **374**, 701–+.

Bałucińska-Church, M., Church, M. J., and Smale, A. P. (2004). The orbital period of the dipping, bursting, globular cluster X-ray source XB 1746-371 from Rossi X-ray Timing Explorer observations. MNRAS, **347**, 334–338.

Baykal, A., Stark, M. J., and Swank, J. (2000). Discovery of the Orbit of the Transient X-Ray Pulsar SAX J2103.5+4545. ApJ, **544**, L129–L132.

Benacquista, M. J. (2002). Relativistic binaries in globular clusters. *Living Reviews in Relativity*, **5**(2).

Callanan, P. J., Grindlay, J. E., and Cool, A. M. (1995). Optical Observations of 4U 1915-05, and the Stability of the Long Term Ephemeris. PASJ, **47**, 153–162.

Carroll, B. W. and Ostlie, D. A. (1996). *An introduction to modern astrophysics*. Reading, MA: Addison-Wesley, —c1996.

Chakrabarty, D., Grunsfeld, J. M., Prince, T. A., Bildsten, L., Finger, M. H., Wilson, R. B., Fishman, G. J., Meegan, C. A., and Paciesas, W. S. (1993). Discovery of the Orbit of the X-ray pulsar OAO 1657-415. ApJ, **403**, L33–L37.

Chevalier, C. and Ilovaisky, S. A. (1977). The binary nature of the LMC X-4 optical candidate. A&A, **59**, L9–L12.

Cominsky, L. R. and Wood, K. S. (1984). Discovery of a 7.1 hour period and eclipses from MXB 1659-29. ApJ, **283**, 765–773.

Corbet, R. (1998). XTE J1855-026. IAU Circ., **6927**, 1–+.

Corbet, R., Barbier, L., Barthelmy, S., Cummings, J., Fenimore, E., Gehrels, N., Hullinger, D., Krimm, H., Markwardt, C., Palmer, D., Parsons, A., Sakamoto, T., Sato, G., and Tueller, J. (2006). Swift/BAT Detection of a 5 hour Period in 4U 1954+31. *The Astronomer's Telegram*, **797**, 1–+.

Corbet, R. H. D., Finley, J. P., and Peele, A. G. (1999). Evidence for a Very Slow X-Ray Pulsar in 2S 0114+650 from Rossi X-Ray Timing Explorer All-Sky Monitor Observations. ApJ, **511**, 876–884.

Corbet, R. H. D., Hannikainen, D. C., and Remillard, R. (2004). The Orbital Period of IGR J19140+098. *The Astronomer's Telegram*, **269**, 1–+.

Courvoisier, T. J.-L., Parmar, A. N., Peacock, A., and Pakull, M. (1986). The discovery of 39 hour periodic dips in the X-ray intensity of XB 1254 - 690. ApJ, **309**, 265–274.

Crampton, D., Cowley, A. P., and Hutchings, J. B. (1980). The probable binary nature of SS 433. ApJ, **235**, L131–L135.

Crampton, D., Hutchings, J. B., and Cowley, A. P. (1985). The supergiant X-ray binary system 2S 0114 + 650. ApJ, **299**, 839–844.

Davison, P. J. N., Watson, M. G., and Pye, J. P. (1977). The binary X-ray pulsar 3U 1538-52. MNRAS, **181**, 73P–79P.

Delgado-Martí, H., Levine, A. M., Pfahl, E., and Rappaport, S. A. (2001). The Orbit of X Persei and Its Neutron Star Companion. ApJ, **546**, 455–468.

den Hartog, P. R., Kuiper, L. M., Corbet, R. H. D., Zand, J. J. M. I., Hermsen, W., Vink, J., Remillard, R., and Klis, M. V. D. (2004). IGR J00370+6122 - A new high-mass X-ray binary. *The Astronomer's Telegram*, **281**, 1–+.

Finley, J. P., Belloni, T., and Cassinelli, J. P. (1992). Periodic outbursts in the peculiar X-ray binary 2S 0114+65. A&A, **262**, L25–L28.

Giacconi, R., Gursky, H., Paolini, F. R., and Rossi, B. B. (1962). Evidence for x rays from sources outside the solar system. *Phys. Rev. Lett.*, **9**(11), 439–443.

Giacconi, R., Gursky, H., Kellogg, E., Schreier, E., and Tananbaum, H. (1971). Discovery of Periodic X-Ray Pulsations in Centaurus X-3 from UHURU. ApJ, **167**, L67+.

Gies, D. R., McSwain, M. V., Riddle, R. L., Wang, Z., Wiita, P. J., and Wingert, D. W. (2002). The Spectral Components of SS 433. ApJ, **566**, 1069–1083.

Grindlay, J. E., Bailyn, C. D., Cohn, H., Lugger, P. M., Thorstensen, J. R., and Wegner, G. (1988). Discovery of a possible X-ray triple - 4U 1915-05. ApJ, **334**, L25–L29.

Haberl, F., Angelini, L., Motch, C., and White, N. E. (1998). X-ray observations of the slowest known Be/X-ray pulsars RXJ0146.9+6121 and XPersei. A&A, **330**, 189–194.

Hannikainen, D. C., Rodriguez, J., and Pottschmidt, K. (2003). Igr J19140+098. IAU Circ., **8088**, 4–+.

Hertz, P. (1987). An 8.5 hour X-ray period in the M15 X-ray source 4U 2129 + 12. ApJ, **315**, L119–L122.

Hertz, P. and Wood, K. S. (1988). Discovery of a 4.2 hour X-ray period in GX 9+9. ApJ, **331**, 764–772.

Holt, S. S., Kaluzienski, L. J., Boldt, E. A., and Serlemitsos, P. J. (1976). A return to the pre-1971 intensity level and a 5.6-d modulation for CYG X-1. Nature, **261**, 213–215.

Hulleman, F., in 't Zand, J. J. M., and Heise, J. (1998). Discovery of the transient X-ray pulsar SAX J2103.5+4545. A&A, **337**, L25–L28.

Hutchings, J. B., Cowley, A. P., Crampton, D., van Paradus, J., and White, N. E. (1979). Centaurus X-3. ApJ, **229**, 1079–1084.

Jones, C., Forman, W., Tananbaum, H., Schreier, E., Gursky, H., Kellogg, E., and Giacconi, R. (1973). Evidence for the Binary Nature of 2u 1700-37. ApJ, **181**, L43+.

Kelley, R. L., Jernigan, J. G., Levine, A., Petro, L. D., and Rappaport, S. (1983). Discovery of 13.5 S X-ray pulsations from LMC X-4 and an orbital determination. ApJ, **264**, 568–574.

Kong, A. K. H., Charles, P. A., Homer, L., Kuulkers, E., and O'Donoghue, D. (2006). Simultaneous X-ray/optical observations of GX9+9 (4U1728-16). MNRAS, **368**, 781–795.

Kubota, A. (1998). X-Ray Determination of the Black-Hole Mass in Cygnus X-1. In K. Koyama, S. Kitamoto, and M. Itoh, editors, *The Hot Universe*, volume 188 of *IAU Symposium*, pages 388–+.

Lang, F. L., Levine, A. M., Bautz, M., Hauskins, S., Howe, S., Primini, F. A., Lewin, W. H. G., Baity, W. A., Knight, F. K., Rotschild, R. E., and Petterson, J. A. (1981). Discovery of a 30.5 day periodicity in LMC X-4. ApJ, **246**, L21–L25.

Levine, A. M. and Corbet, R. (2006). Detection of Additional Periodicities in RXTE ASM Light Curves. *The Astronomer's Telegram*, **940**, 1–+.

Levine, A. M., Bradt, H., Cui, W., Jernigan, J. G., Morgan, E. H., Remillard, R., Shirey, R. E., and Smith, D. A. (1996). First Results from the All-Sky Monitor on the Rossi X-Ray Timing Explorer. ApJ, **469**, L33+.

Levine, A. M., Rappaport, S., Remillard, R., and Savcheva, A. (2004). X1908+075: A Pulsar Orbiting in the Stellar Wind of a Massive Companion. ApJ, **617**, 1284–1295.

Lewin, W. H. G., van Paradijs, J., and van den Heuvel, E. P. J. (1997). *X-ray Binaries*. X-ray Binaries, Edited by Walter H. G. Lewin and Jan van Paradijs and Edward P. J. van den Heuvel, pp. 674. ISBN 0521599342. Cambridge, UK: Cambridge University Press, January 1997.

Lommen, D., Yungelson, L., van den Heuvel, E., Nelemans, G., and Portegies Zwart, S. (2005). Cygnus X-3 and the problem of the missing Wolf-Rayet X-ray binaries. A&A, **443**, 231–241.

Lucke, R., Yentis, D., Friedman, H., Fritz, G., and Shulman, S. (1975). SMC X-1. IAU Circ., **2878**, 2–+.

Makishima, K., Kawai, N., Koyama, K., Shibazaki, N., Nagase, F., and Nakagawa, M. (1984). Discovery of a 437.5-s X-ray pulsation from 4U 1907 + 09. PASJ, **36**, 679–689.

Marshall, F. E. and Takeshima, T. (1998). XTE J1855-026. IAU Circ., **6904**, 2–+.

Marshall, N. and Ricketts, M. J. (1980). Determination of a binary period for the variable X-ray source A1907+09. MNRAS, **193**, 7P–13P.

Mereghetti, S., Stella, L., and de Nile, F. (1993). On the nature of the 25-min periodicity from 4U 0142+614: A nearby, slowly spinning neutron star/Be system? A&A, **278**, L23–L25.

Molina, M., Malizia, A., Bassani, L., Bird, A. J., Dean, A. J., Landi, R., de Rosa, A., Walter, R., Barlow, E. J., Clark, D. J., Hill, A. B., and Sguera, V. (2006). INTEGRAL observations of active galactic nuclei obscured by the Galactic plane. MNRAS, **371**, 821–828.

Muno, M. P., Remillard, R. A., and Chakrabarty, D. (2002). How Do Z and Atoll X-Ray Binaries Differ? ApJ, **568**, L35–L39.

Paczyński, B. (1971). Evolutionary Processes in Close Binary Systems. ARA&A, **9**, 183–+.

Parmar, A. N., White, N. E., Giommi, P., Haberl, F., Pedersen, H., and Mayor, M. (1985). EXO 0748-676. IAU Circ., **4039**, 1–+.

Parmar, A. N., Gottwald, M., van der Klis, M., and van Paradijs, J. (1989). The discovery of 2.93 hour periodic intensity dips from X1323-619. ApJ, **338**, 1024–1032.

Parsignault, D. R., Gursky, H., Kellogg, E. M., Matilsky, T., Murray, S. S., Schreier, E., Tananbaum, H., Giacconi, R., and Brinkman, B. (1972). No X-ray flare seen by Uhuru. Nature, **239**, 123–+.

Pedersen, H., van Paradijs, J., and Lewin, W. H. G. (1981). A four-hour orbital period of the X-ray burster 4U/MXB1636-53. Nature, **294**, 725–727.

Priedhorsky, W. and Terrell, J. (1984). Discovery of a 176 day period in 4U 1820-30. ApJ, **284**, L17–L20.

Ruderman, M. (1976). Crust-breaking by neutron superfluids and the VELA pulsar glitches. ApJ, **203**, 213–222.

Sansom, A. E., Dotani, T., Asai, K., and Lehto, H. J. (1993). Detection of a 5.7-h period in the globular cluster X-ray source 4U 1746-371. MNRAS, **262**, 429–434.

Schaefer, B. E. (1990a). The optical light curve of the low-mass X-ray binary GX 9 + 9. ApJ, **354**, 720–725.

Schaefer, B. E. (1990b). The optical light curve of the low-mass X-ray binary GX 9 + 9. ApJ, **354**, 720–725.

Schreier, E., Giacconi, R., Gursky, H., Kellogg, E., and Tananbaum, H. (1972a). Discovery of the Binary Nature of SMC X-1 from UHURU. ApJ, **178**, L71+.

Schreier, E., Levinson, R., Gursky, H., Kellogg, E., Tananbaum, H., and Giacconi, R. (1972b). Evidence for the Binary Nature of Centaurus X-3 from UHURU X-Ray Observations. ApJ, **172**, L79+.

Seitzer, P., Tuohy, I. R., Mason, K. O., Middleditch, J., Nelson, J., and White, N. E. (1979). S 1822-371. IAU Circ., **3406**, 1–+.

Shivamoggi, V. (2005). X-ray periodicities in sources observed by the RXTE ASM.

Smale, A. P. and Wachter, S. (1999). A Cessation of X-Ray Dipping Activity in X1254-690. ApJ, **527**, 341–344.

Stella, L., Priedhorsky, W., and White, N. E. (1987). The discovery of a 685 second orbital period from the X-ray source 4U 1820 - 30 in the globular cluster NGC 6624. ApJ, **312**, L17–L21.

Szkody, P. and Brownlee, D. E. (1977). AM Herculis - A unique X-ray binary as revealed through the optical light curve. ApJ, **212**, L113–L116.

Tananbaum, H., Gursky, H., Kellogg, E. M., Levinson, R., Schreier, E., and Giacconi, R. (1972). Discovery of a Periodic Pulsating Binary X-Ray Source in Hercules from UHURU. ApJ, **174**, L143+.

Tousey, R., Watanabe, K., and Purcell, J. D. (1951). Measurements of solar extreme ultraviolet and x-rays from rockets by means of a $coso_4$:mn phosphor. *Phys. Rev.*, **83**(4), 792–797.

van Kerkwijk, M. H., Geballe, T. R., King, D. L., van der Klis, M., and van Paradijs, J. (1996). The Wolf-Rayet counterpart of Cygnus X-3. A&A, **314**, 521–540.

Wachter, S., Smale, A. P., and Bailyn, C. (2000). The Reappearance of the Transient Low-Mass X-Ray Binary X1658-298. ApJ, **534**, 367–372.

Watson, M. G., Willingale, R., King, A. R., Grindlay, J. E., and Halpern, J. (1985). U 1624-49. IAU Circ., **4051**, 2–+.

Wen, L., Remillard, R. A., and Bradt, H. V. (2000). X1908+075: An X-Ray Binary with a 4.4 Day Period. ApJ, **532**, 1119–1123.

Wen, L., Levine, A. M., Corbet, R. H. D., and Bradt, H. V. (2006). A Systematic Search for Periodicities in RXTE ASM Data. ApJS, **163**, 372–392.

White, N. E. and Pravdo, S. H. (1979). The discovery of 38.22 second X-ray pulsations from the vicinity of OAO 1653-40. ApJ, **233**, L121–L124.

White, N. E., Mason, K. O., Sanford, P. W., and Murdin, P. (1976). The X-ray behaviour of 3U 0352+30 (X Per). MNRAS, **176**, 201–215.

White, N. E., Becker, R. H., Boldt, E. A., Holt, S. S., Serlemitsos, P. J., and Swank, J. H. (1981). A 5.57 hour modulation of the X-ray flux from 4U 1822-37. ApJ, **247**, 994–1002.

White, N. E., Mason, K. O., Giommi, P., Angelini, L., Pooley, G., Branduardi-Raymont, G., Murdin, P. G., and Wall, J. V. (1987). A 25 min modulation from the vicinity of the unusually soft X-ray source X0142+614. MNRAS, **226**, 645–654.

Ziolkowski, J. (2002). Be/X-ray binaries. *Memorie della Societa Astronomica Italiana*, **73**, 1038–1038.